Cavity-enhanced absorption sensing based on Pound-Drever-Hall sideband locking

Fernanda C. Rodrigues Machado
Department of Physics
McGill University, Montréal, Canada
August 2021

A thesis submitted to McGill University
in partial fulfillment of the requirements
of the degree of
Master of Science

Supervisors: Professor Jack C. Sankey and Professor Lilian I. Childress

Abstract

We present a cavity-enhanced optical absorption measurement technique based on high-bandwidth Pound-Drever-Hall (PDH) sideband locking, which naturally provides a real-time, resonant amplitude quadrature readout that can be mapped onto the cavity's internal loss rate. Cavity-enhancement is widely used in the detection of small signals – an optical cavity traps photons between two highly reflective mirrors, thereby enhancing the effective path length through the absorber [1]. Most of the available techniques, however, probe transmission signals and/or do not provide the stability required for the detection of fast signals.

To ensure optimal enhancement of absorption sensitivity, probe light must be locked on resonance with the cavity. PDH locking relies on phase modulation of a laser beam, creating two sidebands on the original carrier frequency [2]. Upon reflection from a cavity, this modulated light produces a heterodyne signal (beat note) that can be detected and demodulated. We use the phase quadrature of the beat note to lock the cavity on resonance with one of the sidebands, achieving a locking bandwidth in the MHz range that keeps cavity and probe light resonant for hours [3]. Simultaneously, we monitor the amplitude quadrature, which provides a continuous, real-time, heterodyne-amplified readout of the cavity's internal absorption. Our PDH sideband cavity-enhanced absorption readout technique (SideCAR) ensures high sensitivity without reaching saturation limits in the intracavity medium by keeping a relatively low intracavity power, since only one of the sidebands is allowed to enter the cavity, but the signal is boosted above the detector noise by heterodyne detection (using the carrier as a local oscillator).

This thesis presents the theoretical formulation of the sensing technique together with the expressions for the sensitivity limit (ultimately given by the laser quantum noise), and the experimental results from a test cavity setup. Probing a proof-of-concept 5-cm-long Fabry-Perot cavity with a coupled power of 160 μW, we measure an absorption sensitivity of 7×10^{-11} cm$^{-1}/\sqrt{\text{Hz}}$ at 100 kHz (roughly the cavity bandwidth), a factor of 11 from the shot-noise limit. This technique allows the detection of small, transient signals against absorptive backgrounds with sensitivity close to the shot noise limit using a reflection-based measurement in a fairly simple setup, opening the possibility of developing new microscopic single-port real-world sensors for transients, for example using micron-scale optical fiber cavities.

Abrégé

Nous présentons une technique de mesure d'absorption optique améliorée par cavité basée sur le contrôle d'une bande latérale d'un laser via rétroaction Pound-Drever-Hall (PDH) à haute bande passante. Cette technique fournit naturellement une lecture de la quadrature d'amplitude en temps réel, qui peut être mappée sur le taux de perte interne de la cavité. L'amélioration par cavité est largement utilisée dans la détection de faibles signaux: une cavité optique capture des photons entre deux miroirs hautement réfléchissants, augmentant ainsi la longueur du chemin efficace à travers l'absorbeur [1]. Cependant, la plupart des techniques disponibles sondent les signaux de transmission et/ou n'offrent pas la stabilité requise pour la détection de signaux rapides.

Pour assurer une amélioration maximale de la sensibilité d'absorption, la lumière de la sonde doit être fixée en résonance avec la cavité. La technique PDH est basée sur la modulation de phase d'un faisceau laser, formant deux bandes latérales autour de la fréquence du faisceau d'origine [2]. Lors de la réflexion d'une cavité, cette lumière modulée produit un signal hétérodyne qui peut être détecté et démodulé. Nous utilisons la quadrature de phase de ce signal hétérodyne pour fixer la cavité en résonance avec l'une des bandes latérales, obtenant ainsi une stabilité via rétroaction avec une bande passante dans la gamme du MHz qui maintient la cavité et la lumière de la sonde en résonance pendant des heures [3]. En parallèle, nous surveillons la quadrature d'amplitude, qui permet une lecture continue de l'absorption interne de la cavité en temps réel et amplifiée par détection hétérodyne. Notre technique de détection de bande latérale ("SideCAR") assure une sensibilité élevée sans dépasser les limites de saturation dans le milieu intracavité, en gardant la puissance intracavité relativement faible, car une seule des bandes latérales entre dans la cavité, mais le signal est amplifié au-dessus du bruit du détecteur par détection hétérodyne (en utilisant la bande centrale comme oscillateur local).

Cette thèse présente la formulation théorique de la technique de détection ainsi que les expressions de la limite de sensibilité (déterminée ultimement par le bruit quantique du laser), et les résultats expérimentaux obtenus avec une cavité de test. Lors du sondage d'une cavité Fabry-Pérot de 5 cm de long avec une puissance couplée de 160 μW, nous avons mesuré une sensibilité d'absorption de 7×10^{-11} cm$^{-1}/\sqrt{\text{Hz}}$ à 100 kHz (environ la bande passante de la cavité), un facteur 11 au-dessus de la limite de bruit quantique. Cette technique permet la détection de faibles signaux transitoires contre des fonds absorbants avec une sensibilité proche de la limite de bruit quantique en utilisant une mesure basée sur la réflexion et avec une configuration simple, ouvrant la possibilité de développer de nouveaux

capteurs microscopiques à un seul port pour les signaux transitoires, par exemple en utilisant des cavités de fibres optiques à l'échelle du micron.

Acknowledgments

I thank my supervisors Lily and Jack for all the support, help and guidance along these two years. Not only are you great as supervisors, but Lily is also the most inspiring female physicist I could ask to work with (it's beautiful to see your enthusiasm), and Jack's (usual) good mood and jokes (that I actually don't get) made my masters much more enjoyable. Thank you both for all your kindness and for truly caring about me.

To everyone in the QS lab: Jiaxing, Vincent, Simon, Tommy, Pauline, André, Erika, Rigel, Cesar, Michael and Adrian. I am very grateful for all the help with my so many questions, for each of you teaching me so much – starting with how to even run Python, and for creating such a good and friendly environment in our team. I knew from my interview day that this was the best group, and I was not wrong. In fact, you all rank top in any "nice people list".

To my dear friends Ana Paula, Cuco, Elisa, William, Mariana and Isabel, and my dear sister in law Renata for your absolute support when I decided to change careers six years ago, while the rest of the world was calling me crazy. You made all the difference, and I will always be thankful.

To my lovely friends Lenka and Julie, who brought me joy when the world was all messed up in the middle of a pandemic. You are great. To my dear Maura, my step-mother Heloisa, and actually my entire family and my in-laws. The old friends from Brazil and the new friends from Canada. You make me feel loved and motivated every day.

And to my four favourite people: my mother, my father, my brother and my husband. Thank you Mãe for giving me so many opportunities in life and for trusting me so much. Thank you Pai for teaching me from your example to put the best of me in what I do. Thank you Hique for inspiring me to follow dreams and do the things we love. And thank you Bruno for the best advices ever, inspiring stories and for always wanting to see me conquer the world. I say this again, because it's the only truth: all the good things I've ever done were only accomplished because I have the four of you by my side. And it's all worth it. I just hope I tell you enough times how fantastic you are. I love you.

I have so many wonderful friends and the best family of all, that I can comfortably say that I am a very happy woman. You are the reason why I am always smiling. Thank you.

Statement of Contributions

The research carried in this work was supervised by Lilian I. Childress and Jack C. Sankey. Lilian I. Childress, Jack C. Sankey and Shirin A. Enger conceived together the idea of a dosimeter based on the technique described here, and guided me in all steps that led to this dissertation.

Pauline Pestre worked on this project with me, helping in many aspects such as verifying equations, suggesting ideas for next steps and giving me many coding advices. She worked with noise subtraction mentioned in the end of Section 5.4. Pauline Pestre also helped setting up for the acquisition of data showed in Sections 5.2 and 5.4, especially by coding a script for fast data taking. I acquired and analyzed all the data presented in this thesis.

Erika Janitz reviewed my calculations from Chapter 2 and Section 4.2. She also helped with setup alignment and suggested (by doing initial calculations) the different measurements to extract cavity parameters detailed in Section 5.2.

Vincent Dumont contributed with the calculations for intracavity time-varying absorption (Section 3.3). I translated his calculations to our parameters, and investigated the effect of time-modulated absorption on the heterodyne signal V_X (Section 3.3.1).

Liam Scanlon helped setting up the optical table, aligning the cavity and getting the system ready for locking. He also measured the cavity transfer function (which gives the locking bandwidth).

Simon Bernard reviewed the French abstract.

Erika Janitz, Pauline Pestre, Vincent Dumont, Simon Bernard, Jiaxing Ma and Thomas Clark contributed many times with valuable discussions and help setting up the experiment.

Table of Contents

List of Figures

List of Tables

Chapter 1

Introduction

This thesis details work done in the development of a time-resolved cavity-enhanced absorption sensing technique based on Pound-Drever-Hall (PDH) sideband locking. The goal of this project is to measure short-lived, weak absorption signals against an absorptive background using optical cavities. The motivation for developing this new technique originated from radiation dosimetry, where we aim to detect the dose deposited in water via the additional broadband optical absorption induced by solvated electrons created in radiolysis [4, 5], using fiber-based microcavities capable of measuring fast ($\sim \mu$s) transients with access only to reflected signals. Here, we will describe the theory and proof-of-concept experiment that demonstrate an absorption-sensing technique appropriate to this future sensor.

The simplest absorption spectroscopy measurement illuminates a sample with incoming laser intensity I_0 and collects the output intensity I. The Beer-Lambert law $I = I_0 e^{-\alpha d}$ then gives the absorption coefficient α (commonly in units of cm^{-1}), with d corresponding to the path length through the absorber. Often the signal attenuation caused by αd is very small, and the big challenge of absorption spectroscopy is to detect small intensity changes against high background losses and/or experimental technical noise [6]. Optical cavities enhance the absorption signal by trapping resonant light between two highly reflective mirrors, so photons travel back and forth until finally leaking out through one of the mirrors. This increases the effective length over which light interacts with the material of interest by up to twice the number of roundtrips the electric field goes through inside the cavity, or equivalently by a factor of $2\mathcal{F}/\pi$, where $\mathcal{F}$ is the cavity finesse (see Section 2.4). Cavity enhancement is commonly used in spectroscopy, with numerous techniques already adapted for specific applications. These techniques are usually divided in two groups, based on the sensing method: either measuring intensity changes in the signal, or measuring changes in the cavity decay rate (cavity ringdown spectroscopy – CRDS [7–9]). Simple intensity measurements benefit from the $2\mathcal{F}/\pi$ signal enhancement, but are still highly sensitive to laser intensity fluctuations and low frequency technical noise. Some more refined techniques employ frequency-modulation (FM) to encode the signal into higher frequencies. Noise-immune cavity-enhanced optical heterodyne molecular spectroscopy (NICE-OHMS) [10, 11], for example, uses FM at a frequency equal to the cavity free spectral range, so both the carrier and FM sidebands are resonant with the cavity. When one of the bands interacts with an intracavity absorber, the triplet is disturbed, generating a beat note (see Section 4.4). The transmitted beat is intrinsically immune to classical noise, so this technique can provide close to shot-noise-limited measurements of narrow molecular resonances. Demonstrated first by Ye et al. [10] in 1998, NICE-OHMS currently achieves the lowest sensitivity of any absorption-sensing technique (Table 1.1).

The sensitivity of absorption measurements is defined by a noise-equivalent absorption: the smallest absorption coefficient that can be distinguished with a signal-to-noise ratio of 1 during a 1-s measurement interval, usually reported in units of $\mathrm{cm}^{-1}/\sqrt{\mathrm{Hz}}$. The fundamental sensitivity limit is given by the shot noise of the laser. At this limit, every absorption event could be detected, limited only by the uncertainty of occurrence of photon emission [10]. The shot-noise-limited sensitivity for a single-pass absorption measurement $\langle S_\alpha \rangle_{\text{1-pass}}$ is therefore given by

$$\langle S_\alpha \rangle_{\text{1-pass}} = \frac{1}{d}\sqrt{\frac{2e}{\eta P_0}}\,, \tag{1.1}$$

where e is the electron charge, η the detector responsivity (e.g. in A/W) and P_0 the power incident on the absorber. The improvement in sensitivity achieved by different cavity-enhanced sensing modalities will be detailed in Chapter 4. For a given detection time, or equivalently detection bandwidth b, one can calculate the unitless minimum detectable absorption loss (MDAL) by multiplying the sensitivity by $\sqrt{b}$ and absorber path length d (when using optical cavity enhancement, usually d becomes the cavity length L). Table 1.1 shows the reported sensitivity, MDAL and relevant experimental parameters for some previous measurements based on the two methods described above, and compare to our new sideband cavity-enhanced absorption readout (SideCAR) technique (a broader review can be found for example on Refs. [12–14]). Most of the available techniques, however, allow for high sensitivity only under almost ideal conditions, with cavity sizes of tens of cm, non-absorptive intra-cavity media and lossless mirrors. There is still room for the development of new techniques looking for high sensitivity detection of concentration of species under non-ideal conditions, e.g. transient signals immersed in highly absorptive background media.

We describe a single-laser, single-modulator, weak-probe approach appropriate to detecting both narrow and broadband transient absorption signals optimally suited to a one-sided cavity (access to reflection only). To ensure that the probe light is always

Technique	Sensitivity ($\mathrm{cm}^{-1}/\sqrt{\mathrm{Hz}}$)	MDAL	L (cm)	$\mathcal{F}$	P_{in}	P_{circ}
NICE-OHMS [10]	1×10^{-14}	5.2×10^{-13}	50	100 000	9.5 mW†	300 W
Locked cw-CRDS [15]	8.8×10^{-12}	-	42*	12 500†	25 mW	100 W†
Swept cw-CRDS [9]	2.5×10^{-9}	1.4×10^{-7}	45	7 420	-	-
Off-axis ICOS [16]	1.9×10^{-12}	-	110	-	-	-
CEAMLAS [17]	2.6×10^{-10}	1.6×10^{-7}	20	1 000	-	-
Opt feedback CEAS [18]	5.7×10^{-11}	-	49	144 000	-	-
CE-DCS [19]	2×10^{-10}	-	60	$\sim$4 000	3.6 mW	$\sim$4 W†
SideCAR [this work]	7×10^{-11}	1.1×10^{-7}	5	9 000	160 µW‡	520 mW

Table 1.1: Comparison of reported sensitivity, MDAL, cavity length L, finesse $\mathcal{F}$, input power P_{in} and circulating power P_{circ} between different cavity-enhanced absorption sensing techniques. NICE-OHMS: noise-immune cavity-enhanced optical heterodyne molecular spectroscopy. CRDS: cavity ring-down spectroscopy. ICOS: integrated cavity output spectroscopy. CEAMLAS: cavity enhanced amplitude modulated laser absorption spectroscopy. CEAS: cavity-enhanced absorption spectroscopy. CE-DCS: cavity-enhanced dual comb spectroscopy. SideCAR: sideband cavity-enhanced absorption readout. *Roundtrip length. †Estimate (calculated from other stated values, assuming lossless symmetric cavities). ‡Coupled input power (corresponding to the power in one phase-modulation sideband). Dashes mean values are not stated.

on resonance with the cavity (necessary to detect transients), we employ a high-speed PDH locking scheme [3], based on phase-modulation and posterior demodulation with a reference signal, and we take advantage of the other demodulation quadrature (amplitude quadrature) to measure cavity absorption. This signal varies with intracavity absorption, providing cavity information without requiring access to a second optical port. Under ideal circumstances, this heterodyne reflection measurement presents the same shot-noise-limited sensitivity as a typical transmission measurement when considering cavities of same finesse with the same circulating power. In addition, it allows the shift of the signal of interest to higher frequencies (due to the frequency modulation and heterodyne detection), where the detector noise is lower. When compared to transmission-based heterodyne approaches (e.g. NICE-OHMS [10, 11]) or amplitude-modulated reflection measurements (e.g. CEAMLAS [17, 20]), it permits operation with much lower intra-cavity power for a given shot-noise-limited sensitivity. We demonstrate the proof-of-concept in a cm-scale, finesse 9000 testbed cavity, achieving a sensitivity of 10^{-10} $\mathrm{cm}^{-1}/\sqrt{\mathrm{Hz}}$ without optimization over a 30-200 kHz frequency range with a coupled power of 160 μW (from a total of 3.5 mW incident power). A minimal sensitivity of 7×10^{-11} cm$^{-1}/\sqrt{\text{Hz}}$ is achieved around 100 kHz, a factor of 11 above shot noise.

This thesis is divided in a theoretical part (Chapters 2 to 4) and a second part describing the experiment (Chapter 5). We start by deriving the cavity model and cavity equations in the high-finesse limit in Chapter 2. We then study the heterodyne PDH reflection signal that gives rise to the two signals used for (i) locking (phase quadrature V_Y) and (ii) sensing (amplitude quadrature V_X) in Chapter 3, and derive the effects of intracavity time-varying absorption on the cavity output field and the signal of interest V_X. This is especially important for our goal of detecting transients, allowing us to understand the measurement bandwidth. Chapter 4 gives the derivation of the sensitivity limit of our technique compared to other absorption sensing modalities. We then turn to our testbed experimental setup in Chapter 5, describing the apparatus and the set of measurements used to extract cavity parameters. Finally, Section 5.4 illustrates our experimental results for the sensitivity of the sideband absorption readout technique. We conclude the thesis in Chapter 6, discussing briefly the future directions we can see for the project.

Chapter 2

Cavity model

We begin by deriving the Fabry-Pérot cavity equations to be used throughout this thesis, using the transfer matrix model to obtain the cavity amplitude reflection and transmission. From that, we write down the equation for finesse ($\mathcal{F}$) in a lossy cavity and analyze the cavity equations in the limit of high finesse (highly reflective mirrors and low losses), an approximation that represents well our experiment. Finally, we verify that an optical cavity provides an enhancement of absorption signals equal to $2\mathcal{F}/\pi$.

2.1 Cavity reflection and transmission

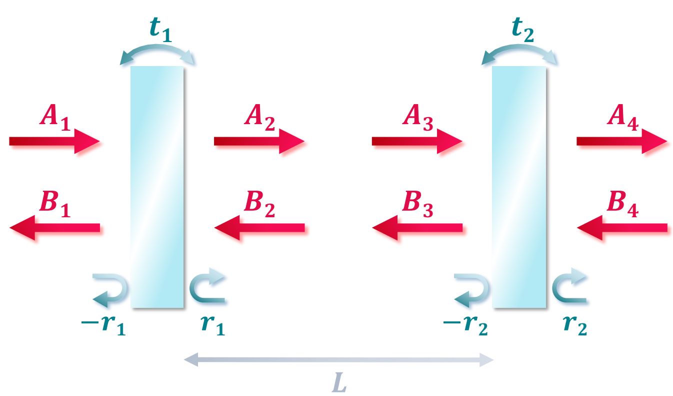

Figure 2.1: Fields in an optical cavity. The Fabry-Pérot cavity is made of two mirrors facing each other. Laser light enters the cavity via the input mirror (with amplitude reflection and transmission coefficients r_1 and t_1) and leaks out either via the input mirror or the back mirror (with amplitude reflection and transmission coefficients r_2 and t_2). The optical field at the j^{th} location ($j = 1, 2, 3, 4$ represents each of the mirrors' surfaces from left (mirror 1) to right (mirror 2)) is given by $A_j e^{i((x-x_j)\tilde{n}_j\omega/c+\omega t)} + B_j e^{i((x-x_j)\tilde{n}_j\omega/c+\omega t)}$, where x is the spatial position of the field along the cavity axis (perpendicular to the mirrors), x_j is the position of each mirror surface, $\tilde{n}_j$ is the complex refractive index of the j^{th}-position medium and ω is the laser frequency.

A simple way to model the optical cavity is by considering the incoming and out-going optical fields at each side of both mirrors. From Fig. 2.1,

$$\begin{aligned} A_2 &= A_1 t_1 + B_2 r_1 \\ B_1 &= B_2 t_1 - A_1 r_1 \ , \end{aligned} \tag{2.1}$$

where A_j and B_j are forward- and backward-propagating field amplitudes and r_i and t_i are the (real) mirror reflection and transmission amplitude coefficients ($i = 1$ for the input mirror and $i = 2$ for the back mirror). Solving these for A_2 and B_2, we get

$$\begin{bmatrix} A_2 \\ B_2 \end{bmatrix} = \boldsymbol{M}_1 \begin{bmatrix} A_1 \\ B_1 \end{bmatrix} \ , \tag{2.2}$$

where

$$\boldsymbol{M}_1 = \frac{1}{t_1} \begin{bmatrix} r_1^2 + t_1^2 & r_1 \\ r_1 & 1 \end{bmatrix} \tag{2.3}$$

is the transfer matrix representing the effects in the electric field due to the input mirror [21]. The back mirror transfer matrix $\boldsymbol{M}_2$ can be found by the same process. We assume lossless mirrors ($r_i^2 + t_i^2 = 1$) and model cavity intrinsic losses by a zero-thickness scattering layer added to each mirror [22], represented by multiplying the mirror matrices by the matrix

$$\boldsymbol{M}_S = \begin{bmatrix} e^{-\delta/4} & 0 \\ 0 & e^{\delta/4} \end{bmatrix} \ , \tag{2.4}$$

where δ represents the unitless intrinsic power losses per half of a round trip (i.e. per pass) in the cavity. Extrinsic absorption is modelled by letting the (wavelength dependent) refractive index $\tilde{n}$ of the intracavity medium be complex,

$$\tilde{n} = n + i\frac{\alpha c}{2\omega} \ , \tag{2.5}$$

where n is the real refractive index, c is the speed of light, ω the laser frequency and α represents the extrinsic power losses per unit length (units of inverse length). The intracavity field change per pass is then given by

$$E_{\text{1-pass}} = E_0 e^{iL\tilde{n}\omega/c} = E_0 e^{iLn\omega/c} e^{-\frac{\alpha}{2}L} \ , \tag{2.6}$$

where E_0 is the initial field amplitude. The propagation of the field is represented by the intracavity matrix:

$$\boldsymbol{I} = \begin{bmatrix} e^{iLn\omega/c - \frac{\alpha}{2}L} & 0 \\ 0 & e^{-iLn\omega/c + \frac{\alpha}{2}L} \end{bmatrix} \ . \tag{2.7}$$

The full cavity transfer matrix $\boldsymbol{C}$ is then equal to

$$\boldsymbol{C} = \boldsymbol{M_2} \cdot \boldsymbol{M_S} \cdot \boldsymbol{I} \cdot \boldsymbol{M_S} \cdot \boldsymbol{M_1} \tag{2.8}$$

where

$$\begin{bmatrix} A_4 \\ B_4 \end{bmatrix} = \begin{bmatrix} \boldsymbol{C}_{11} & \boldsymbol{C}_{12} \\ \boldsymbol{C}_{21} & \boldsymbol{C}_{22} \end{bmatrix} \cdot \begin{bmatrix} A_1 \\ B_1 \end{bmatrix} . \tag{2.9}$$

For a normally incident field A_1 (with no backward incident field $B_4 = 0$), the cavity fractional reflected and transmitted fields are given by

$$r(\omega) = \frac{E_r}{E_{\text{in}}} = -\frac{\boldsymbol{C}_{21}}{\boldsymbol{C}_{22}} = \frac{r_2 t_1^2}{e^{\delta+\alpha L - \frac{2iLn\omega}{c}} - r_1 r_2} - r_1 \tag{2.10}$$

$$t(\omega) = \frac{E_t}{E_{\text{in}}} = \boldsymbol{C}_{11} - \frac{\boldsymbol{C}_{12}\boldsymbol{C}_{21}}{\boldsymbol{C}_{22}} = \frac{t_1 t_2 e^{\frac{\delta+\alpha L}{2} - \frac{iLn\omega}{c}}}{e^{\delta+\alpha L - \frac{2iLn\omega}{c}} - r_1 r_2} , \tag{2.11}$$

and the fractional reflected and transmitted powers (reflectance R and transmittance T) are:

$$R(\omega) = \left|\frac{E_r}{E_{\text{in}}}\right|^2 = |r(\omega)|^2 = \frac{r_1^2 e^{2(\delta+\alpha L)} + r_2^2 - 2r_1 r_2 e^{\delta+\alpha L}\cos(2Ln\omega/c)}{e^{2(\delta+\alpha L)} + r_1^2 r_2^2 - 2r_1 r_2 e^{\delta+\alpha L}\cos(2Ln\omega/c)} \tag{2.12}$$

$$T(\omega) = \left|\frac{E_t}{E_{\text{in}}}\right|^2 = |t(\omega)|^2 = \frac{t_1^2 t_2^2 e^{\delta+\alpha L}}{e^{2(\delta+\alpha L)} + r_1^2 r_2^2 - 2r_1 r_2 e^{\delta+\alpha L}\cos(2Ln\omega/c)} . \tag{2.13}$$

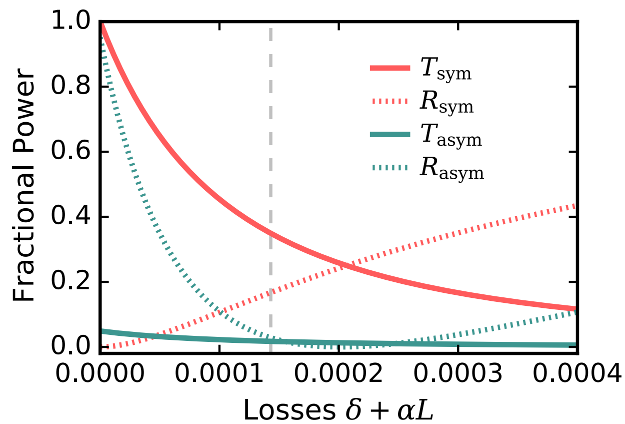

Figure 2.2: Cavity fractional power reflection and transmission versus cavity losses $\delta + \alpha L$, for resonant light. Teal curves represent an asymmetric cavity with mirrors of fractional transmission $t_1^2 = 407$ ppm and $t_2^2 = 5$ ppm. Coral curves represent a symmetric cavity of the same finesse ($t_1^2 = t_2^2 = 206$ ppm). The vertical dashed line marks the intrinsic losses of our empty cavity ($\mathcal{F}(\alpha = 0) = 9006$ and $\delta = 143$ ppm)

To study the change induced by absorption in the power of a resonant beam leaking through a cavity, we plot in Fig. 2.2 the fractional reflected and transmitted power versus intracavity losses, for the cases of an asymmetric cavity (with mirrors with transmissivities equal to those in our experiment) and a symmetric cavity of the same finesse. The slope at $\alpha = 0$ tells us how much transmission or reflection changes as the absorption changes. This slope is related to absorption measurement sensitivity, as we will see in Chapter 4. We can observe that there is no information in reflected power at critical coupling (zero slope), although there is still information in the phase of the reflected light.

2.2 Finesse in a lossy cavity

The equation for finesse in a lossy cavity can be derived by expanding transmission (Eq. 2.13) around a resonance peak (i.e., when the detuning $\Delta\omega$ between laser light ω and a cavity mode goes to zero) to find the cavity linewidth κ (defined as the FWHM of the transmission peak, in units of rad/s). Cavity finesse $\mathcal{F}$ is then given by

$$\mathcal{F} \equiv \frac{\omega_{\mathrm{FSR}}}{\kappa} \tag{2.14}$$

$$= \frac{e^{(\delta+\alpha L)/2}\pi\sqrt{r_1 r_2}}{e^{\delta+\alpha L} - r_1 r_2} \tag{2.15}$$

where $\omega_{\mathrm{FSR}} = \pi c/(Ln)$ is the cavity free spectral range in rad/s.

2.3 The high finesse limit

In the high finesse limit, defined by low transmissivity mirrors and small cavity losses ($t_1^2, t_2^2, \delta, \alpha L \ll 1$), we can make some approximations and write the cavity equations in terms of cavity parameters $\mathcal{F}$ or τ, where $\tau \equiv 1/\kappa$ is the cavity power decay rate or cavity lifetime. In this limit[1] (and substituting $r_i = \sqrt{1 - t_i^2}$), Eq. 2.15 can be written as

$$\mathcal{F} \approx \frac{\pi}{\frac{t_1^2}{2} + \frac{t_2^2}{2} + \delta + \alpha L} \tag{2.16}$$

[1] The approximations are truncated to

$$\mathcal{O}\left(\frac{\delta + \alpha L}{2}\right)^1 + \mathcal{O}\left(\frac{t_1}{2}\right)^2 + \mathcal{O}\left(\frac{t_2}{2}\right)^2 + \mathcal{O}(\delta + \alpha L)^2 + \mathcal{O}(t_1 t_2)^2 + \mathcal{O}(t_1)^4 + \mathcal{O}(t_2)^4 \ .$$

and from Eq. 2.14, the cavity lifetime is

$$\tau \approx \frac{Ln}{c(\frac{t_1^2}{2} + \frac{t_2^2}{2} + \delta + \alpha L)} \ . \tag{2.17}$$

Expanding for small detuning $\Delta\omega = |\omega - \omega_c|$ from a cavity mode ω_c, the cavity equations (Eqs. 2.10 to 2.13) become[2]

$$r(\Delta\omega) \approx \frac{t_1^2}{2\pi\left(\frac{1}{2\mathcal{F}} - i\frac{\Delta\omega}{\omega_{\mathrm{FSR}}}\right)} - r_1 \tag{2.18}$$

$$t(\Delta\omega) \approx \frac{t_1 t_2}{2\pi\left(\frac{1}{2\mathcal{F}} - i\frac{\Delta\omega}{\omega_{\mathrm{FSR}}}\right)} \tag{2.19}$$

$$R(\Delta\omega) \approx \frac{t_1^4 - 2\pi r_1 t_1^2/\mathcal{F}}{4\pi^2\left(\frac{1}{4\mathcal{F}^2} + \frac{\Delta\omega^2}{\omega_{\mathrm{FSR}}^2}\right)} + r_1^2 \tag{2.20}$$

$$T(\Delta\omega) \approx \frac{t_1^2 t_2^2}{4\pi^2\left(\frac{1}{4\mathcal{F}^2} + \frac{\Delta\omega^2}{\omega_{\mathrm{FSR}}^2}\right)} \ . \tag{2.21}$$

For a resonant beam ($\Delta\omega \to 0$), these simplify to

$$r_{\mathrm{res}} \approx \frac{\mathcal{F} t_1^2}{\pi} - r_1 \tag{2.22}$$

$$t_{\mathrm{res}} \approx \frac{\mathcal{F} t_1 t_2}{\pi} \tag{2.23}$$

$$R_{\mathrm{res}} \approx \frac{(\mathcal{F} t_1^2 - \pi r_1)^2}{\pi^2} \tag{2.24}$$

$$T_{\mathrm{res}} \approx \frac{\mathcal{F}^2 t_1^2 t_2^2}{\pi^2} \ , \tag{2.25}$$

and the cavity fractional circulating power $\rho_{\mathrm{circ}} = P_{\mathrm{circ}}/P_{\mathrm{in}}$ (P_{circ} is the cavity circulating power just next to the input mirror and $P_{\mathrm{in}} \equiv |E_{\mathrm{in}}|^2$ is the incoming power[3]) is given by

$$\rho_{\mathrm{circ}} \approx \frac{\mathcal{F}^2 t_1^2}{\pi^2} \ . \tag{2.26}$$

Figure 2.3 illustrates the validity of the high $\mathcal{F}$ approximation for the mirrors used in our experiment ($t_1^2 \approx 407$ ppm and $t_2^2 \approx 5$ ppm).

[2]Neglecting terms of second order in power losses and detune from cavity resonance.

[3]Technically, the power P in an electric field $E = E_0 e^{i\omega t}$ is proportional to the time-averaged field, i.e. $P \propto \langle \mathrm{Re}\{E\}^2 \rangle \propto E_0^2/2$ [23]. For simplicity, however, throughout this thesis we renormalize the field amplitude so that $P = E^* E$.

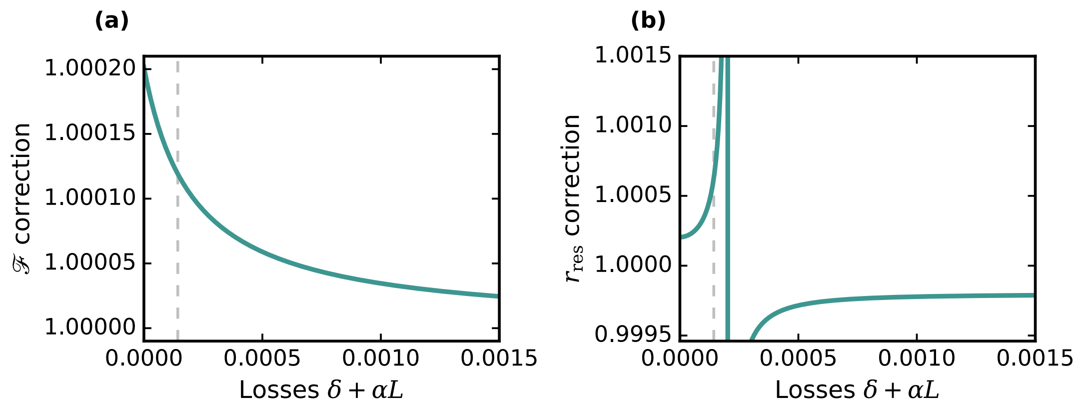

Figure 2.3: Corrections on finesse and cavity fractional amplitude reflection in the high finesse approximation for varying cavity losses $\delta + \alpha L$, plotted for mirrors with fractional transmission $t_1^2 = 407$ ppm and $t_2^2 = 5$ ppm (similar to the ones used in our experiment). The curves show the ratio between the high $\mathcal{F}$ approximation and no approximations. (a) Correction on cavity finesse, given by the ratio between Eq. 2.16 and Eq. 2.15. (b) Correction for cavity amplitude reflection, given by the ratio between Eq. 2.22 and Eq. 2.10 for a resonant beam. Vertical dashed lines mark the experimental cavity intrinsic losses $\delta = 143$ ppm.

2.4 Cavity enhancement

Here we study the enhancement provided by an optical cavity to the change in optical power of a laser beam passing through an absorber. Let's look at the change in signal (δP) due to absorption compared to the signal without absorption (signal contrast $\delta P/P$), in the cases of free space and cavity-enhanced transmission measurements (assuming $\alpha L \ll 1$) [24]. For an absorber in free space,

$$\frac{P_{\mathrm{out}}}{P_{\mathrm{in}}} = e^{-\alpha L} \approx 1 - \alpha L \quad \text{and} \quad \frac{\delta P_{\mathrm{out}}}{P_{\mathrm{out},\alpha=0}} = -\alpha L \ , \tag{2.27}$$

where P_{in} is the incoming laser power and P_{out} is the power just after the absorber. Now, when the absorber is inside an optical cavity, $P_{\mathrm{out}} \to P_T$, where P_T is the power transmitted by the cavity. If we substitute Eq. 2.16 in Eq. 2.25 and expand for small αL,

$$\frac{P_T}{P_{\mathrm{in}}} \approx \frac{t_1^2 t_2^2}{\left(\frac{t_1^2}{2} + \frac{t_2^2}{2} + \delta\right)^2} - \frac{2 t_1^2 t_2^2 \alpha L}{\left(\frac{t_1^2}{2} + \frac{t_2^2}{2} + \delta\right)^3} \quad \text{and} \tag{2.28}$$

$$\frac{\delta P_T}{P_{T,\alpha=0}} = -\frac{2\alpha L}{\frac{t_1^2}{2} + \frac{t_2^2}{2} + \delta} = -\frac{2\mathcal{F}\alpha L}{\pi} \ . \tag{2.29}$$

Comparing Eqs. 2.27 and 2.29, we finally get the cavity enhancement

$$\frac{\delta P_T}{P_{T,\alpha=0}} \Big/ \frac{\delta P_{\text{out}}}{P_{\text{out},\alpha=0}} = \frac{2\mathcal{F}}{\pi} \ . \tag{2.30}$$

Note that the enhancement given by Eq. 2.30 is only true if the beam is on resonance with the cavity and its linewidth is narrow in comparison to the cavity linewidth κ.

Alternately, we can find the same enhancement by considering the effective length of the cavity, as determined by the cavity power decay time τ. After m intracavity roundtrips, the transmitted field can be written as[4]

$$E_t = (r_1 r_2 e^{-\delta-\alpha L})^m E_{\text{1-pass}} \tag{2.31}$$

$$\approx \left(e^{-\frac{t_1^2}{2}-\frac{t_2^2}{2}-\delta-\alpha L}\right)^m E_{\text{1-pass}} \tag{2.32}$$

where $E_{\text{1-pass}} = E_0 e^{(-\delta-\alpha L)/2} t_1 t_2$ is the transmitted field after a single pass. We know that

$$\tau = \frac{Ln}{c(\frac{t_1^2}{2} + \frac{t_2^2}{2} + \delta + \alpha L)} \quad \text{and} \quad t_{\text{rt}} = \frac{2Ln}{c} \ , \tag{2.33}$$

where t_{rt} is the time for one roundtrip. Substituting Eq. 2.33 into Eq. 2.32,

$$E_t = e^{-t_{\text{rt}} m/(2\tau)} E_{\text{1-pass}} \ . \tag{2.34}$$

Note that the amplitude decay time is 2τ. Finally,

$$2\tau = \frac{2Lnm}{c} = \frac{nL_{\text{eff}}}{c} \ , \tag{2.35}$$

where L_{eff} is the absorber effective length. Substituting $\tau = \mathcal{F}/\omega_{\text{FSR}} = \mathcal{F}Ln/(\pi c)$,

$$\frac{L_{\text{eff}}}{L} = \frac{2\mathcal{F}}{\pi} \ . \tag{2.36}$$

[4] Using $r_i \approx 1 - \frac{t_i^2}{2}$.

Chapter 3

Heterodyne reflection locking and sensing

Our sensing technique relies on collecting and demodulating the optical heterodyne beat signal generated upon reflection of a phase-modulated beam from an optical cavity. A phase-modulated beam can be seen as a signal having three dominant frequency components: a carrier at the original laser frequency, and two sidebands detuned from the carrier by the modulation frequency. When only one modulation sideband interacts with an optical cavity (which can happen in the resolved-sideband limit), the triplet is disturbed, generating a beat between the interacting sideband and the non-interacting carrier (i.e., phase modulation is converted into amplitude modulation). In the following section we derive the expressions for the reflection of the phase-modulated light and explain how we use the resulting amplitude-modulated signal (heterodyne beat note) to lock our cavity on resonance with one of the sidebands [2, 3]. We then show how we use the out-of-phase quadrature[5] of this same signal to detect changes in intracavity absorption. This locked measurement is capable of detecting transient signals with a detection bandwidth determined by the cavity amplitude decay rate $1/(4\pi\tau)$, as we investigate at the end of this chapter.

3.1 Pound-Drever-Hall sideband locking

Pound-Drever-Hall locking [2] is based on phase-modulation (PM) of an incoming laser beam, represented by

$$E_{\mathrm{in,PM}} = \sqrt{P_{\mathrm{in}}} e^{i(\omega_l t + \beta \sin(\Omega t))} \tag{3.1}$$

where P_{in} is the average incoming laser power, ω_l is the original laser frequency, β the modulation amplitude and Ω the modulation frequency. For small β, the phase-modulated field can be written as

$$E_{\mathrm{in,PM}} \approx \sqrt{P_{\mathrm{in}}} \left(e^{i\omega_l t} \sqrt{\rho_{\mathrm{c}}} - e^{i(\omega_l - \Omega)t} \sqrt{\rho_{\mathrm{sb}}} + e^{i(\omega_l + \Omega)t} \sqrt{\rho_{\mathrm{sb}}} \right) \ , \tag{3.2}$$

[5]Shifted by $\pi/2$ with respect to the modulation signal.

which can be treated as an incoming beam with a carrier at frequency ω_l and relative amplitude $\sqrt{\rho_c} \approx 1$ (in the limit where the approximation is valid), and two sidebands at frequencies $\omega_l \pm \Omega$ and relative amplitudes $\sqrt{\rho_{sb}} \approx \beta/2$. Upon reflection from an optical cavity, the outgoing reflected field $E_{r,\mathrm{PM}}$ becomes:

$$E_{r,\mathrm{PM}} \approx \sqrt{P_{\mathrm{in}}}\left(e^{i\omega_l t}\sqrt{\rho_{\mathrm{c}}}\; r(\omega_l) - e^{i(\omega_l-\Omega)t}\sqrt{\rho_{\mathrm{sb}}}\; r(\omega_l-\Omega) + e^{i(\omega_l+\Omega)t}\sqrt{\rho_{\mathrm{sb}}}\; r(\omega_l+\Omega)\right) \tag{3.3}$$

and the reflected power $P_{R,\mathrm{PM}}$:

$$\begin{aligned} P_{R,\mathrm{PM}} \approx\; & \underbrace{P_{\mathrm{in}}\left(\rho_{\mathrm{c}} r^2(\omega_l) + \rho_{\mathrm{sb}} r^2(\omega_l-\Omega) + \rho_{\mathrm{sb}} r^2(\omega_l+\Omega)\right)}_{\mathrm{DC}} \\ & + \underbrace{P_{\mathrm{in}}\sqrt{\rho_{\mathrm{c}}\rho_{\mathrm{sb}}}\{-r(\omega_l)r^*(\omega_l-\Omega) + r(\omega_l)r^*(\omega_l+\Omega) - r^*(\omega_l)r(\omega_l-\Omega) + r^*(\omega_l)r(\omega_l+\Omega)\}}_{P_X}\cos(\Omega t) \\ & + \underbrace{iP_{\mathrm{in}}\sqrt{\rho_{\mathrm{c}}\rho_{\mathrm{sb}}}\{-r(\omega_l)r^*(\omega_l-\Omega) - r(\omega_l)r^*(\omega_l+\Omega) + r^*(\omega_l)r(\omega_l-\Omega) + r^*(\omega_l)r(\omega_l+\Omega)\}}_{P_Y}\sin(\Omega t) \\ & + (\text{terms oscillating in } 2\Omega)\;, \end{aligned} \tag{3.4}$$

with $r(\omega)$ given by Eq. 2.10.

The cosine and sine terms in Eq. 3.4 can be seen as two quadratures of a beat note oscillating at frequency Ω, while the constant (DC) terms represent the average reflected power. Figure 3.1 illustrates these three distinct terms for varying cavity resonance frequency. As we can see from Fig. 3.1c, the phase quadrature[6] P_Y varies linearly close to resonance. In the PDH sideband locking scheme [3], we park one of the sidebands on resonance with the cavity and use P_Y as an error signal, feeding it back to a voltage-controlled oscillator (VCO) that controls the sideband detuning frequency Ω, thereby keeping the sideband locked to the cavity (see Fig. 5.1).

3.2 Sideband cavity-enhanced absorption readout (SideCAR)

When one of the sidebands (say the one at $\omega_l - \Omega$) is resonant with the cavity, its amplitude reflection coefficient $r(\omega_l - \Omega) = r_{\mathrm{res}}$ is real-valued and given by Eq. 2.22. If the other bands are far from resonance (valid if $\Omega \gg \kappa$), their amplitude reflection coefficients

[6] In-phase with the modulation signal $\propto \sin(\Omega t)$ (Eq. 3.1).

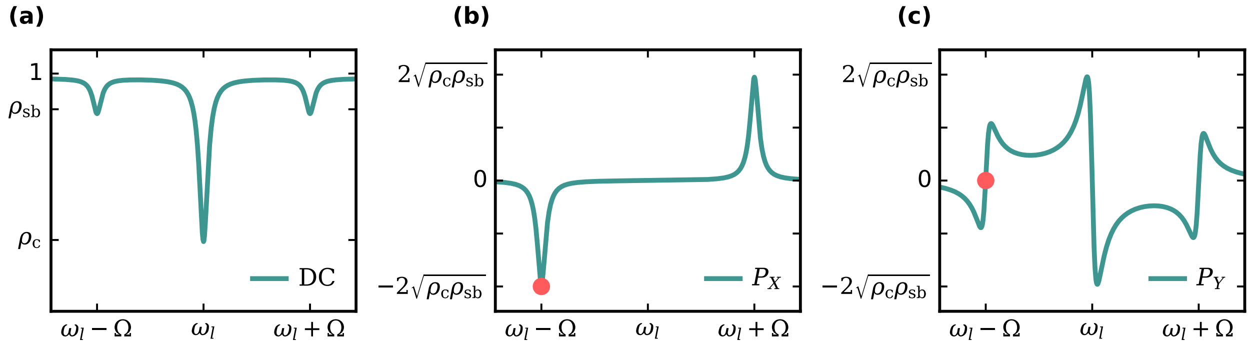

Figure 3.1: Reflection of phase-modulated light (Eq. 3.4) vs. cavity resonance frequency, plotted for a cavity of $\mathcal{F} = 150$ and normalized for input power P_{in}. (a) DC terms (average reflected power). (b) Amplitude quadrature P_X; and (c) phase quadrature P_Y of the PDH reflection beat note. Red dots indicate the lower sideband resonance, which is used as the lock-point.

are given simply by $-r_1$. As indicated by the red dot in Fig. 3.1c, the phase quadrature P_Y in Eq. 3.4 goes to zero, and the reflected power becomes:

$$P_{R,\text{PMsb}} \approx \underbrace{P_{\text{in}}\left(\rho_c r_1^2 + \rho_{\text{sb}}(r_1^2 + r_{\text{res}}^2)\right)}_{\text{DC}} + \underbrace{2P_{\text{in}}\sqrt{\rho_c\rho_{\text{sb}}}\left(r_1^2 + r_1 r_{\text{res}}\right)}_{P_X}\cos(\Omega t)\ . \tag{3.5}$$

Equation 3.5 and Fig. 3.1b show that the heterodyne beat generated in PDH reflection provides a non-zero signal at a sideband resonance. Moreover, this signal depends on r_{res}, which depends on cavity finesse $\mathcal{F}$ and therefore varies with intracavity absorption α. Substituting Eq. 2.22 into Eq. 3.5, we find that exactly on sideband resonance the out-of-phase quadrature amplitude becomes:

$$P_{X,\text{sb}} \approx 2P_{\text{in}}\sqrt{\rho_c\rho_{\text{sb}}}\frac{\mathcal{F}t_1^2}{\pi}\ . \tag{3.6}$$

So, by locking the cavity to a sideband using the phase quadrature P_Y of the optical heterodyne beat note, we can use the amplitude quadrature P_X to monitor changes in intracavity absorption in real time.

As will be detailed in Chapter 5, the measured signal is actually a voltage amplitude $V_X = G_X P_X$ retrieved by demodulating a $\pi/2$-shifted portion of the beat with a local oscillator coming from the modulation signal ($\propto \sin(\Omega t)$ according to Eq. 3.1), where G_X contains all the gains involved in the detection scheme. From Eq. 3.6, the signal V_X is proportional to $\sqrt{\rho_c\rho_{\text{sb}}}$. Remembering that we work on the resolved sideband regime (i.e., modulation frequency Ω much larger than the laser and the cavity linewidths) and also allow only one sideband to interact with the cavity by having $\Omega \neq \omega_{\text{FSR}}$, this means that we can take advantage of a strong carrier signal ρ_c to boost the weak sideband signal ρ_{sb}.

Since the cavity is locked on resonance with the laser light, this technique also allows us to detect transient signals. The detection bandwidth for transients is investigated in the next section, and the technique sensitivity floor will be discussed in Section 4.2.

3.3 Cavity response to modulated absorption

As described in the previous sections, the absorption detection scheme presented in this thesis involves collecting and demodulating the amplitude quadrature of the Pound-Drever-Hall reflection beatnote (P_X), while keeping one phase-modulation sideband locked on resonance to the cavity. This generates the voltage signal $V_X \equiv G_X P_X$ (where G_X is a gain factor in V/W), which is sensitive to changes in intracavity absorption α according to Eqs. 2.16 and 3.6. Our goal now is to understand the changes in V_X due to time-varying intracavity absorption (transients) to determine the bandwidth of our measurement scheme. We will find that when α varies with time at a certain frequency $\omega_\alpha/2\pi$, V_X will fluctuate at this same modulation frequency, with an amplitude that is filtered by the cavity low-pass behaviour with cutoff frequency $1/(4\pi\tau)$, where τ is the cavity lifetime.

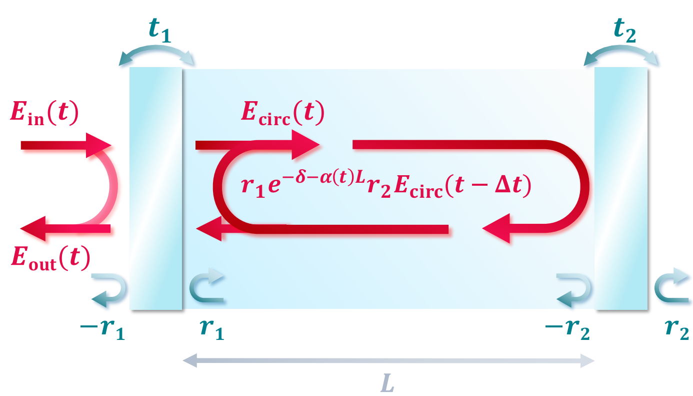

Figure 3.2: Incoming ($E_{\text{in}}(t)$), circulating ($E_{\text{circ}}(t)$) and out-going ($E_{\text{out}}(t)$) fields in a lossy cavity. The cavity losses are separated in intrinsic (δ) and time-varying extrinsic ($\alpha(t)L = \alpha_0 L \cos(\omega_\alpha t)$) amplitude losses per roundtrip. r_i and t_i represent the i^{th} mirror amplitude reflection and transmission coefficients, respectively, and L is the cavity length.

A classical version of the input-output formalism is used to derive the cavity response to time-varying intracavity absorption (transients). The following derivation assumes that the changes in intracavity absorption are slow when compared to the cavity round-trip time. We start by deriving an equation of motion for the intracavity field (defined just to the right of the input mirror – Fig. 3.2). At time t, the circulating field is given by the incident field transmitted by the front mirror $t_1 E_{\mathrm{in}}(t)$ plus the recirculating field from a time $t - \Delta t$ before:

$$E_{\mathrm{circ}}(t) = t_1 E_{\mathrm{in}}(t) + r_1 r_2 e^{-\delta - \alpha(t)L} E_{\mathrm{circ}}(t - \Delta t) \tag{3.7}$$

$$\approx t_1 E_{\mathrm{in}}(t) + \left(1 - \frac{t_1^2}{2} - \frac{t_2^2}{2} - \delta - \alpha(t)L\right) E_{\mathrm{circ}}(t - \Delta t) \tag{3.8}$$

where again we assume lossless mirrors with amplitude reflectivity and transmissivity r_i and t_i, δ contains the cavity intrinsic losses (power loss per pass), $\alpha(t)$ represents the time-varying extrinsic absorption (power loss per unit length) and $\Delta t = 2Ln/c$ is the roundtrip time (L is the cavity length, n the intracavity medium refractive index and c the speed of light). We assume low transmissivity mirrors and low losses $t_1, t_2, \delta, \alpha L \ll 1$. Equation 3.8 can be written as a differential equation:

$$\frac{E_{\mathrm{circ}}(t) - E_{\mathrm{circ}}(t - \Delta t)}{\Delta t} = \frac{t_1 E_{\mathrm{in}}(t) - \left(\frac{t_1^2}{2} + \frac{t_2^2}{2} + \delta + \alpha(t)L\right) E_{\mathrm{circ}}(t - \Delta t)}{\Delta t} \tag{3.9}$$

$$\Rightarrow \frac{dE_{\mathrm{circ}}(t)}{dt} \approx -\frac{c\left(\frac{t_1^2}{2} + \frac{t_2^2}{2} + \delta + \alpha(t)L\right) E_{\mathrm{circ}}(t)}{2Ln} + \frac{c t_1 E_{\mathrm{in}}(t)}{2Ln} \quad (\text{for } \Delta t \to 0)\ , \tag{3.10}$$

following the assumption that the fluctuations in $\alpha(t)$ and $E_{\mathrm{in}}(t)$ are much slower than the round-trip time. We can write Eq. 3.10 in terms of the cavity loss rate (cavity linewidth $\kappa = 1/\tau$, in rad/s), separating this rate in different loss ports, namely κ_{in} corresponding to the input mirror transmission loss, κ_0 corresponding to scattering and back mirror transmission losses, and $\kappa_\alpha(t)$ corresponding to the time-varying extrinsic absorption. From Eq. 2.17, in the high finesse limit, we have:

$$\kappa(t) = \frac{c t_1^2}{2Ln} + \frac{c\left(t_2^2 + 2\delta\right)}{2Ln} + \frac{c\alpha(t)L}{Ln} \tag{3.11}$$

$$\equiv \kappa_{\mathrm{in}} + \kappa_0 + \kappa_\alpha(t)\ . \tag{3.12}$$

Substituting Eq. 3.12 into Eq. 3.10, we have

$$\frac{dE_{\mathrm{circ}}(t)}{dt} = -\frac{\kappa_{\mathrm{in}} + \kappa_0 + \kappa_\alpha(t)}{2} E_{\mathrm{circ}}(t) + \sqrt{\frac{\kappa_{\mathrm{in}} c}{2Ln}} E_{\mathrm{in}}(t)\ . \tag{3.13}$$

We now let the time-varying absorption be a sinusoidal function at frequency ω_α ($\alpha(t)L \to \alpha_0 L \cos(\omega_\alpha t)$), which will cause a sinusoidal variation in the circulating and output fields. Our goal is to investigate how the fluctuation in the output is related to $\alpha(t)$. Assuming the fluctuations are small, the circulating field can be treated as a mean value at the laser frequency and a small fluctuating term due to the modulated absorption, $E_{\text{circ}}(t) = \bar{E}_{\text{circ}} + \Delta E_{\text{circ}}(t)$:

$$\frac{d\left(\bar{E}_{\text{circ}} + \Delta E_{\text{circ}}(t)\right)}{dt} = -\frac{\kappa_{\text{in}} + \kappa_0 + \kappa_\alpha(t)}{2}\left(\bar{E}_{\text{circ}} + \Delta E_{\text{circ}}(t)\right) + \sqrt{\frac{\kappa_{\text{in}} c}{2Ln}}\bar{E}_{\text{in}} \ , \tag{3.14}$$

where we also assume no such fluctuations in the incoming field ($\Delta E_{\text{in}}(t) = 0$; note that we work in the frame rotating at the cavity resonance frequency ω_c). Keeping only the time-varying terms, we have:

$$\frac{d\left(\Delta E_{\text{circ}}(t)\right)}{dt} = -\frac{\kappa_{\text{in}} + \kappa_0}{2}\Delta E_{\text{circ}}(t) - \frac{\kappa_\alpha(t)}{2}\left(\bar{E}_{\text{circ}} + \Delta E_{\text{circ}}(t)\right) \tag{3.15}$$

$$\approx -\frac{\kappa_{\text{in}} + \kappa_0}{2}\Delta E_{\text{circ}}(t) - \frac{\kappa_\alpha(t)}{2}\bar{E}_{\text{circ}} \qquad (\text{for } |\Delta E_{\text{circ}}(t)| \ll \bar{E}_{\text{circ}}) \ . \tag{3.16}$$

Substituting $\kappa_\alpha(t) = c\alpha_0 \cos(\omega_\alpha t)/n$ and going to the frequency domain,[7]

$$-i\omega\Delta E_{\text{circ}}(\omega) = -\frac{\kappa_{\text{in}} + \kappa_0}{2}\Delta E_{\text{circ}}(\omega) - \Big(\delta(\omega - \omega_\alpha) + \delta(\omega + \omega_\alpha)\Big)\frac{c\alpha_0}{4n}\bar{E}_{\text{circ}} \tag{3.17}$$

$$\Rightarrow \Delta E_{\text{circ}}(\omega) = -\underbrace{\frac{1}{-i\omega + \frac{\kappa_{\text{in}}+\kappa_0}{2}}}_{\chi(\omega)}\Big(\delta(\omega - \omega_\alpha) + \delta(\omega + \omega_\alpha)\Big)\frac{c\alpha_0}{4n}\bar{E}_{\text{circ}} \tag{3.18}$$

where $\delta(\omega \pm \omega_\alpha)$ is the Dirac delta function, and we defined the cavity susceptibility $\chi(\omega) \equiv 1/(-i\omega + \frac{\kappa_{\text{in}}+\kappa_0}{2})$. So $\Delta E_{\text{circ}}(\omega)$ is nonzero only at $\pm\omega_\alpha$. $\bar{E}_{\text{circ}}$ can be found from the time-independent terms of Eq. 3.14:

$$0 = -\frac{\kappa_{\text{in}} + \kappa_0}{2}\bar{E}_{\text{circ}} + \sqrt{\frac{\kappa_{\text{in}} c}{2Ln}}\bar{E}_{\text{in}} \tag{3.19}$$

$$\Rightarrow \bar{E}_{\text{circ}} = \underbrace{\frac{2}{\kappa_{\text{in}} + \kappa_0}}_{\chi(0)}\sqrt{\frac{\kappa_{\text{in}} c}{2Ln}}\bar{E}_{\text{in}} \ . \tag{3.20}$$

Substituting Eq. 3.20 in Eq. 3.18,

$$\Delta E_{\text{circ}}(\omega) = -\chi(\omega)\Big(\delta(\omega - \omega_\alpha) + \delta(\omega + \omega_\alpha)\Big)\frac{c\alpha_0}{4n}\chi(0)\sqrt{\frac{\kappa_{\text{in}} c}{2Ln}}\bar{E}_{\text{in}} \ . \tag{3.21}$$

[7] We use the following convention for the Fourier transform of a function $f(t)$:

$$FT\{f(t)\} = f(\omega) = \frac{1}{2\pi}\int_{-\infty}^{+\infty} f(t)e^{i\omega t}dt \ .$$

The cavity reflected field is given by:

$$E_r(t) = -r_1 E_{\text{in}}(t) + t_1 E_{\text{circ}}(t) \tag{3.22}$$

$$= -r_1 \bar{E}_{\text{in}} + t_1 \left(\bar{E}_{\text{circ}} + \Delta E_{\text{circ}}(t)\right) \ . \tag{3.23}$$

Going to the frequency domain, substituting Eqs. 3.20 and 3.21 and $t_1 = \sqrt{\kappa_{\text{in}} 2Ln/c}$ (Eq. 3.12),

$$E_r(\omega) = -r_1 \bar{E}_{\text{in}} + t_1 \left(\bar{E}_{\text{circ}} + \Delta E_{\text{circ}}(\omega)\right) \tag{3.24}$$

$$\Rightarrow E_r(0) = \left(-r_1 + \kappa_{\text{in}} \chi(0)\right) \bar{E}_{\text{in}} \tag{3.25}$$

$$E_r(\pm\omega_\alpha) = -\kappa_{\text{in}} \chi(0) \chi(\pm\omega_\alpha) \frac{c\alpha_0}{4n} \bar{E}_{\text{in}} \ . \tag{3.26}$$

Since these are Fourier components in the frame rotating at the laser frequency, the outgoing reflected field will have a carrier at the cavity resonance frequency ω_c and two sidebands detuned by the absorber frequency ω_α ($\omega_c \pm \omega_\alpha$). On Fig. 3.3a-b, we plot the magnitude and phase of $E_r(\omega_\alpha)$ (Eq. 3.26), and we can observe that the cavity acts as a low-pass filter with cutoff frequency $\omega_{\text{cutoff}} = (\kappa_{\text{in}} + \kappa_0)/2 \equiv 1/2\tau$ for intracavity modulated absorption.

3.3.1 Changes in V_X due to time-varying absorption

To get an expression for the time-modulated $V_X(t)$, we have to account for the phase-modulation of the incoming laser beam, i.e., include the promptly reflected, off-resonant carrier and (upper) sideband, and lock the other (lower) sideband on resonance with the cavity ($\omega_c \to \omega_l - \Omega$). From Eq. 3.2, the incoming field can be written as

$$E_{\text{in,PM}}(t) = E_0 e^{i\omega_l t} \sqrt{\rho_{\text{c}}} + E_0 e^{i(\omega_l + \Omega)t} \sqrt{\rho_{\text{sb}}} - E_0 e^{i(\omega_l - \Omega)t} \sqrt{\rho_{\text{sb}}} \tag{3.27}$$

where now we let the incoming field be a fast-varying function of time with amplitude E_0. Upon reflection from the cavity, having the lower sideband locked on resonance and the intracavity field time-modulated by transient absorption, the outgoing field becomes

$$\begin{aligned} E_{r,\text{PMsb}}(t) = &-r_1 E_0 \left(e^{i\omega_l t} \sqrt{\rho_{\text{c}}} + e^{i(\omega_l + \Omega)t} \sqrt{\rho_{\text{sb}}}\right) \\ &- \Big(-r_1 E_0 + t_1 \left(\bar{E}_{\text{circ}} + \Delta E_{\text{circ}}(t)\right)\Big) e^{i(\omega_l - \Omega)t} \sqrt{\rho_{\text{sb}}} \ . \end{aligned} \tag{3.28}$$

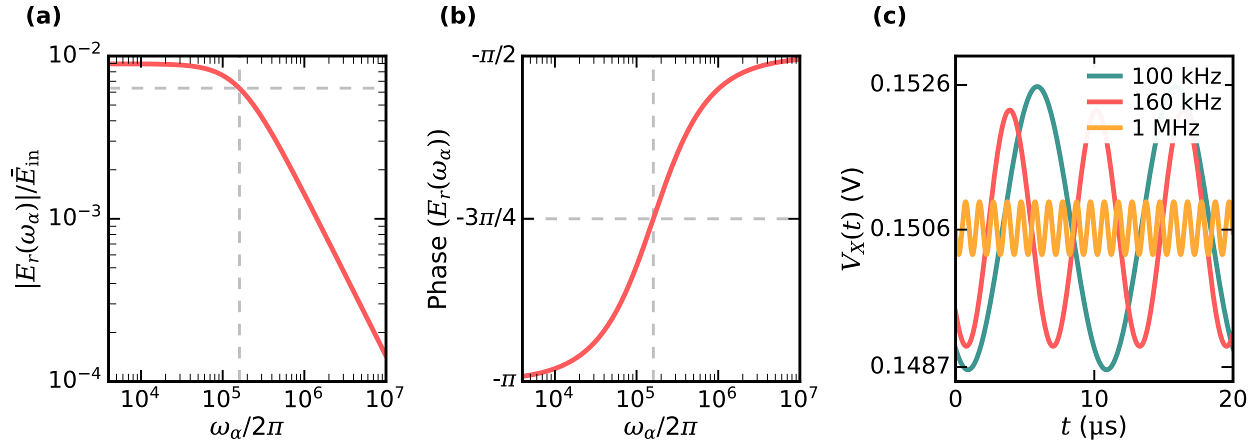

Figure 3.3: Modulated intracavity absorption. (a) Magnitude and (b) phase of the outgoing absorption modulation sideband $E_r(\omega_\alpha)$ (Eq. 3.26) as a function of the absorption modulation frequency $\omega_\alpha/2\pi$. We observe the cavity low-pass behaviour with cutoff frequency $1/4\pi\tau = 160$kHz (vertical dotted lines). Horizontal dotted lines mark the -3 dB point in magnitude and $3\pi/4$ phase-shift. (c) $V_X(t)$ (Eq. 3.31), plotted for three different absorber frequencies $\omega_\alpha/2\pi$: 100 kHz (teal), 160 kHz (coral) and 1 MHz (yellow). Again we can observe the filtering effect of the cavity to the detection of the fluctuating absorption signal. Plotted for the experimental parameters $G, P_{\rm in}, \rho_{\rm c}, \rho_{\rm sb}, r_1, r_2, \tau, L, n, \delta$ discussed in Chapter 5 and $\alpha_0 = 10^{-6}$ cm^{-1}.

We can find $\Delta E_{\rm circ}(t)$ by taking the inverse Fourier transform of Eq. 3.21:

$$\Delta E_{\rm circ}(t) = -\left(e^{i\omega_\alpha t}\chi(-\omega_\alpha) + e^{-i\omega_\alpha t}\chi(\omega_\alpha)\right)\frac{c\alpha_0}{4n}\chi(0)\sqrt{\frac{\kappa_{\rm in}c}{2Ln}}E_0\ . \tag{3.29}$$

Substituting Eqs. 3.20 and 3.29 into Eq. 3.28, noting that $-r_1 + \kappa_{\rm in}\chi(0) = r_{\rm res}$,

$$\begin{aligned} E_{r,\rm PMsb}(t) = &-r_1 E_0\left(e^{i\omega_l t}\sqrt{\rho_{\rm c}} + e^{i(\omega_l+\Omega)t}\sqrt{\rho_{\rm sb}}\right) - r_{\rm res}E_0 e^{i(\omega_l-\Omega)t}\sqrt{\rho_{\rm sb}} \\ &+ (r_1 + r_{\rm res})E_0\sqrt{\rho_{\rm sb}}\ \frac{c\alpha_0}{4n}\left(e^{i(\omega_l-\Omega+\omega_\alpha)t}\chi(-\omega_\alpha) + e^{i(\omega_l-\Omega-\omega_\alpha)t}\chi(\omega_\alpha)\right). \end{aligned} \tag{3.30}$$

We finally find $V_X(t)$ by first calculating $P_{R,\rm PMsb}(t) = E_{r,\rm PMsb}(t)^* E_{r,\rm PMsb}(t)$, collecting it with a photodetector, shifting by $\pi/2$ and mixing with a reference at $\sin(\Omega t)$. Neglecting terms oscillating at $\geq \Omega$,

$$\begin{aligned} V_X(t) = -G_X P_{\rm in} 2\sqrt{\rho_{\rm c}\rho_{\rm sb}}\, r_1\,(r_1 + r_{\rm res})\Big(1 &- \left(\chi(-\omega_\alpha) + \chi(\omega_\alpha)\right)\frac{c\alpha_0}{4n}\cos(\omega_\alpha t) \\ &- \left(\chi(-\omega_\alpha) - \chi(\omega_\alpha)\right)\frac{c\alpha_0}{4n} i\sin(\omega_\alpha t)\Big) \end{aligned} \tag{3.31}$$

where G_X is the gain of the detector and mixer circuits and $P_{\text{in}} \equiv E_0^2$. We conclude that intracavity time-modulated absorption adds a fluctuating term at the absorption modulation frequency ω_α to V_X, which is filtered by the cavity behaving as a low-pass with cutoff frequency $1/2\tau$, determined by the cavity susceptibility $\chi(\pm\omega_\alpha) = 1/\left(\frac{1}{2\tau} \mp i\omega_\alpha\right)$ (Fig. 3.3c).

Chapter 4

Shot-noise-limited sensitivity

In this chapter, we derive the theoretical noise floor (given by the shot-noise limit) of our PDH sideband-lock absorption signal (a heterodyne reflection measurement), and compare it to that of simple reflection, simple transmission and heterodyne transmission signals. We will emphasize the $\sqrt{2}$ advantage of a conventional reflection sensing scheme compared to conventional transmission sensing setups, and the $\sqrt{2}$ disadvantage of heterodyne detection compared to average power (DC) detection.

The shot-noise-limited sensitivity $\langle S_\alpha \rangle$ of an absorption measurement (in units of inverse length per square root frequency) is given by the photocurrent shot noise at the detector $\langle S_i \rangle$ [25] scaled by the derivative of the signal i_{signal} with respect to absorption,

$$\langle S_\alpha \rangle = \frac{\langle S_i \rangle}{|d(i_{\text{signal}})/d\alpha|} \ , \tag{4.1}$$

where the shot noise comes from the time-averaged power at the detector $\bar{P}_{\text{d}}$,

$$\langle S_i \rangle = \sqrt{2e\eta \bar{P}_{\text{d}}} \tag{4.2}$$

(e is the electron charge and η is the detector responsivity in A/W). In the following derivations, we will also explicitly consider imperfect mode-matching to the cavity by introducing a power coupling parameter ϵ, where $\epsilon = 1$ corresponds to perfect cavity coupling. This coupling parameter has to be considered since the promptly reflected uncoupled power adds noise to the detector in reflection-based measurements.

The sensitivity calculation for heterodyne detection can be approached by two different, equivalent ways. We can consider that the detector outputs a DC signal with amplitude proportional to the RMS of the heterodyne beat, and the current noise is just proportional to the square root of the average power reaching the detector $\bar{P}_{\text{d}}$. For simplicity, this is the chosen approach for this section. Alternately, we can consider the detection through a mixing circuit (what actually happens in our apparatus – see Chapter 5). A high-bandwidth detector outputs an AC voltage proportional to the beat power, which is then mixed with a reference at the same frequency. The mixer outputs a signal proportional to the beat amplitude, but the noise is amplified by a factor of $\sqrt{2}$ (the power noise gets doubled). In both the cases, the sensitivity floor $\langle S_\alpha \rangle$ of heterodyne detection increases by a factor of $\sqrt{2}$ when compared to simple detection.

4.1 Simple reflection measurement

We first study the case of a simple reflection measurement when unmodulated laser light is resonant with the cavity. The power $\bar{P}_{\rm d}$ reaching the detector is the reflection of both uncoupled and coupled terms, while the signal comes from the coupled, resonant mode:

$$\langle S_i \rangle_R = \sqrt{2e\eta P_{\rm in}\left((1-\epsilon)r_1^2 + \epsilon r_{\rm res}^2\right)} \tag{4.3}$$

$$i_{{\rm signal},R} = \eta\epsilon P_{\rm in} r_{\rm res}^2 \tag{4.4}$$

where $r_{\rm res}$ is given by Eq. 2.22. Equations 4.1 and 4.2 give:

$$\langle S_\alpha \rangle_R = \frac{\pi^2}{\mathcal{F}^2 L t_1^2} \frac{\sqrt{(1-\epsilon)r_1^2 + \epsilon r_{\rm res}^2}}{r_{\rm res}\epsilon\sqrt{2P_{\rm in}}} \sqrt{\frac{e}{\eta}}. \tag{4.5}$$

In the limit of high reflectivity and small losses (i.e., r_1 and $r_{\rm res} \approx 1$, so that $\bar{P}_{\rm d} \approx P_{\rm in}$), Eq. 4.5 becomes

$$\langle S_\alpha \rangle_R \approx \frac{\pi^2}{\mathcal{F}^2 L t_1^2} \frac{1}{\epsilon\sqrt{2P_{\rm in}}} \sqrt{\frac{e}{\eta}} \tag{4.6}$$

$$\approx \frac{\pi}{2\mathcal{F} L} \frac{1}{\epsilon\sqrt{2P_{\rm in}}} \sqrt{\frac{e}{\eta}} \qquad (\text{for } \delta \to 0,\ t_1^2 \to 2\pi/\mathcal{F})\ . \tag{4.7}$$

In terms of circulating power $P_{\rm circ} = \rho_{\rm circ}\epsilon P_{\rm in}$ ($\rho_{\rm circ}$ given by Eq. 2.26), Eqs. 4.5 and 4.6 become

$$\langle S_\alpha \rangle_R = \frac{\pi}{\mathcal{F} L t_1} \frac{\sqrt{(1-\epsilon)r_1^2 + \epsilon r_{\rm res}^2}}{r_{\rm res}\sqrt{2\epsilon P_{\rm circ}}} \sqrt{\frac{e}{\eta}} \tag{4.8}$$

$$\approx \frac{\pi}{\mathcal{F} L t_1} \frac{1}{\sqrt{2\epsilon P_{\rm circ}}} \sqrt{\frac{e}{\eta}}\ . \tag{4.9}$$

4.2 Heterodyne reflection measurement – SideCAR

We now study the case of heterodyne detection when one sideband is locked on resonance with the cavity and the other sideband and the carrier are off-resonant (resolved sideband limit), which is the measurement technique described in this thesis (see Chapter 3). In our heterodyne reflection detection, the average power at the detector $\bar{P}_{\mathrm{d}}$ is given by the uncoupled reflected power plus the coupled DC terms in Eq. 3.5, and i_{signal} is proportional to the RMS (see Page 21) of the detected beatnote (term at $\cos(\Omega t)$ in Eq. 3.5),

$$\langle S_i \rangle_{\mathrm{SideCAR}} = \sqrt{2e\eta P_{\mathrm{in}}((1-\epsilon)r_1^2 + \epsilon(\rho_{\mathrm{c}} r_1^2 + \rho_{\mathrm{sb}}(r_1^2 + r_{\mathrm{res}}^2))} \tag{4.10}$$

$$i_{\mathrm{signal,SideCAR}} = \eta\epsilon 2 P_{\mathrm{in}} \sqrt{\rho_{\mathrm{c}}\rho_{\mathrm{sb}}}(r_1^2 + r_1 r_{\mathrm{res}}) \sqrt{\langle \cos(\Omega t)^2 \rangle} \tag{4.11}$$

$$= \eta\epsilon\sqrt{2} P_{\mathrm{in}} \sqrt{\rho_{\mathrm{c}}\rho_{\mathrm{sb}}}(r_1^2 + r_1 r_{\mathrm{res}}) \ . \tag{4.12}$$

If we assume high reflectivity input mirror $r_1 \approx 1$ and small modulation amplitude $\rho_{\mathrm{sb}} \to 0$, so that the total average power at the detector is $\approx P_{\mathrm{in}}$, we then have the measurement sensitivity:

$$\langle S_\alpha \rangle_{\mathrm{SideCAR}} = \frac{\pi^2}{\mathcal{F}^2 L t_1^2} \frac{1}{\epsilon\sqrt{P_{\mathrm{in}}\rho_{\mathrm{c}}\rho_{\mathrm{sb}}}} \sqrt{\frac{e}{\eta}} \tag{4.13}$$

$$\approx \frac{\pi}{2\mathcal{F} L} \frac{1}{\epsilon\sqrt{P_{\mathrm{in}}\rho_{\mathrm{c}}\rho_{\mathrm{sb}}}} \sqrt{\frac{e}{\eta}} \qquad (\text{for } \delta \to 0,\ t_1^2 \to 2\pi/\mathcal{F}) \ . \tag{4.14}$$

In terms of circulating power $P_{\mathrm{circ}} = \rho_{\mathrm{circ}}\epsilon\rho_{\mathrm{sb}} P_{\mathrm{in}}$ (with ρ_{circ} given by Eq. 2.26, and noting that now only one sideband is coupled to the cavity), Eq. 4.13 becomes

$$\langle S_\alpha \rangle_{\mathrm{SideCAR}} = \frac{\pi}{\mathcal{F} L t_1} \frac{1}{\sqrt{\epsilon P_{\mathrm{circ}}\rho_{\mathrm{c}}}} \sqrt{\frac{e}{\eta}} \ . \tag{4.15}$$

4.3 Simple transmission measurement

In this case, the signal that carries absorption information is equal to the total power reaching the detector, so the photocurrent shot noise and signal current are given simply by

$$\langle S_i \rangle_T = \sqrt{2e\eta\epsilon P_{\mathrm{in}} t_{\mathrm{res}}^2} \tag{4.16}$$

$$i_{\mathrm{signal},T} = \eta\epsilon P_{\mathrm{in}} t_{\mathrm{res}}^2 \tag{4.17}$$

where $t_{\rm res}$ is given by Eq. 2.23. Note that transmission measurements are commonly performed using a symmetric cavity[8] ($r_1 = r_2$), and reflection measurements typically use single-sided cavities ($r_2 \to 1$). To avoid confusion, we will from now on represent symmetric cavity mirrors by $\tilde{r}_i$ and $\tilde{t}_i$, while r_i and t_i represent single-sided cavity mirrors. To get cavities with same finesse, we use $\tilde{r}_1 = \tilde{r}_2 = \sqrt{r_1 r_2}$. Equations 4.1 and 4.2 give:

$$\langle S_\alpha \rangle_T = \frac{\pi^2}{\mathcal{F}^2 L \tilde{t}_1 \tilde{t}_2} \frac{1}{\sqrt{2\epsilon P_{\rm in}}} \sqrt{\frac{e}{\eta}} \tag{4.18}$$

$$\approx \frac{\pi}{\mathcal{F} L} \frac{1}{\sqrt{2\epsilon P_{\rm in}}} \sqrt{\frac{e}{\eta}} \qquad (\text{for } \delta \to 0,\ \tilde{t}_1 \tilde{t}_2 \to \pi/\mathcal{F}) \ . \tag{4.19}$$

In terms of circulating power $P_{\rm circ} = \rho_{\rm circ} \epsilon P_{\rm in}$, Eq. 4.18 becomes

$$\langle S_\alpha \rangle_T = \frac{\pi}{\mathcal{F} L \tilde{t}_2} \frac{1}{\sqrt{2 P_{\rm circ}}} \sqrt{\frac{e}{\eta}} \ . \tag{4.20}$$

4.3.1 Comparing simple reflection to simple transmission

The ratio between Eqs. 4.9 and 4.20 given by

$$\left(\frac{\langle S_\alpha \rangle_R}{\langle S_\alpha \rangle_T} \right)_{P_{\rm circ}} = \frac{1}{\sqrt{2\epsilon}} \tag{4.21}$$

(where we use $\tilde{t}_2 = \sqrt{1 - r_1 r_2} \approx t_1/\sqrt{2}$ for $t_1 \to 0$) confirms the intuition that, for cavities of the same finesse and with the same circulating power, a conventional reflection measurement (single-sided cavity) performs better than a conventional transmission measurement (symmetric cavity) by a factor of $\sqrt{2}$, since in the double-sided cavity we lose information from the input port, while collecting only what leaves from the back mirror. This advantage however depends on good coupling between laser and cavity, since uncoupled power adds noise to the reflection detector. Transmission measurements through reversed asymmetric cavity ($r_1 \to 1$) achieve the same sensitivity as an ideal reflection measurement.

[8] One could claim that the best transmission measurement would be achieved by using a single-sided cavity with $r_1 \to 1$ (inverted mirrors when compared to optimized reflection measurements). This would result in a sensitivity better by a factor of $\sqrt{2}$ when compared to the double-sided cavity transmission (Eqs. 4.18 and 4.20 divided by $\sqrt{2}$). However, to build up the same circulating power as the double-sided simple transmission cavity, the inverted asymmetric one would need an incoming power $P_{\rm in}$ many times larger, which may not be easily achievable experimentally. For a cavity of $\mathcal{F} \approx 9000$ and intrinsic power losses $\delta \approx 140$ ppm (similar to our experiment parameters – Section 5.2), that would require an incoming power > 40 times larger! Comparing to the circulating power inside the asymmetric sideband reflection cavity (say we would just swap the mirrors in our apparatus), this $\sqrt{2}$ improvement in sensitivity would still require ~ 5 times more incoming laser power.

4.3.2 Comparing SideCAR to simple transmission

Comparing the shot-noise limited sensitivity for a single-sided cavity probed using our sideband-based technique (Eq. 4.15, where we assumed small losses and small modulation amplitude so that $\bar{P}_\mathrm{d} \approx P_\mathrm{in}$) to the shot-noise-limited sensitivity for a double-sided cavity probed by transmission on resonance (Eq. 4.20) for measurements with same cavity finesse and same circulating power, we get

$$\left(\frac{\langle S_\alpha \rangle_\mathrm{SideCAR}}{\langle S_\alpha \rangle_T}\right)_{P_\mathrm{circ}} = \frac{\sqrt{2}\tilde{t}_2}{t_1\sqrt{\epsilon\rho_\mathrm{c}}} \tag{4.22}$$

$$= \frac{1}{\sqrt{\epsilon\rho_\mathrm{c}}} \, , \tag{4.23}$$

again using $\tilde{t}_2 \approx t_1/\sqrt{2}$ for the case of cavities with same finesse. Equation 4.23 immediately shows that the sensitivity of our technique (Eqs. 4.13 and 4.15) is comparable to that of transmission-based strategies. As shown in Fig. 4.1, in an ideal case of high finesse, perfect coupling efficiency, low sideband power ρ_sb, and minimal loss in the path between cavity and reflection detector (which can be achieved with a circulator), the two measurements present the same sensitivity floor.

From Eq. 4.21, a simple reflection measurement from a single-sided cavity provides sensitivity better than transmission (from a double-sided cavity) by a factor of $\sqrt{2}$. This advantage is lost in heterodyne detection, since in this case the noise is increased by $\sqrt{2}$ when mixing down (see Page 21). Imperfect cavity coupling adds uncoupled power to the reflection measurement, thus increasing its shot noise, while not affecting the transmission measurement. Similar results to the ideal case are obtained if we use the actual mirror reflectivities and sideband power employed in our experiment. Our technique is thus comparable to transmission-based methods while also permitting a high-bandwidth lock and single-port geometry that may be advantageous for real-world devices.

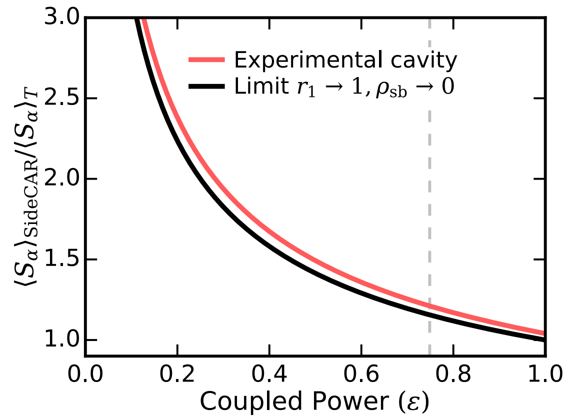

Figure 4.1: Comparing the sensitivity of our SideCAR technique (sideband reflection from a single-sided cavity) $\langle S_\alpha \rangle_{\rm SideCAR}$ to that acquired with a simple symmetric cavity transmission measurement $\langle S_\alpha \rangle_T$ for varying cavity coupling, for cavities of same finesse and same circulating power. Black curve shows the ratio in an ideal case of $r_1,\ \rho_{\rm c} \to 1$ and $\rho_{\rm sb} \to 0$. Coral curve shows the sensitivity ratio for our experimental cavity parameters ($r_1 \approx 0.999796,\ r_2 \approx 0.9999974,\ \rho_{\rm c} \approx 0.8831,\ \rho_{\rm sb} \approx 0.0590$), assuming perfect collection of reflected power. Dashed vertical line marks the fractional coupled power in our experiment ($\epsilon \approx 0.749$). For a fixed circulating power, transmission measurements are insensitive to coupling. The promptly reflected uncoupled light adds noise to the reflection detector though, bringing the noise floor up.

4.4 Heterodyne transmission measurement – NICE-OHMS

NICE-OMHS [10, 11] is a noise-immune spectroscopy technique that collects a heterodyne transmission signal from a phase-modulated laser. We consider it here for comparison purposes, since it is a well-known and widely-employed spectroscopy technique that uses a similar phase modulation approach. The incoming field is again given by Eq. 3.2, but the modulation frequency Ω is chosen to be a multiple of the cavity free spectral range, so that the carrier and two sidebands are all resonant with the cavity. There is no beat signal if all three bands are equally disturbed, but if the absorption spectrum is narrower than Ω, then only one of the bands interacts with the intracavity sample and a heterodyne signal is generated in transmission.

Traditionally, to get the maximum sensitivity, the carrier interacts with the sample, which yields a heterodyne signal twice as high as that given by a sideband interaction. Upon interaction with a sample resonance, the carrier goes through a phase shift ϕ, giving a dispersion signal. However, to compare NICE-OHMS to our heterodyne reflection technique without too many approximations in the final result usually given in literature, I here derive the NICE-OHMS sensitivity by looking at an absorption signal, instead of dispersion. Since we know there is no absorption beat signal when the carrier interacts with the sample, we instead analyze the case of a sample resonant with the lower sideband.

When the lower sideband interacts with a sample resonance, the cavity transmitted field is given by

$$E_{\mathrm{NICEsb}} = \sqrt{\epsilon P_{\mathrm{in}}}(\sqrt{\rho_{\mathrm{c}}}e^{i\omega_l t}t_{\mathrm{res},\alpha=0} - \sqrt{\rho_{\mathrm{sb}}}e^{i(\omega_l-\Omega)t}t_{\mathrm{res},\alpha\neq 0} + \sqrt{\rho_{\mathrm{sb}}}e^{i(\omega_l+\Omega)t}t_{\mathrm{res},\alpha=0}) \tag{4.24}$$

where t_{res} is the cavity amplitude transmission coefficient (Eq. 2.23) for the non-interacting ($\alpha = 0$) and interacting ($\alpha \neq 0$) modes.

The output power P_{NICEsb}, neglecting terms at 2Ω, becomes:

$$P_{\mathrm{NICEsb}} = \epsilon P_{\mathrm{in}}((\rho_{\mathrm{c}} + \rho_{\mathrm{sb}})t^2_{\mathrm{res},\alpha=0} + \rho_{\mathrm{sb}}t^2_{\mathrm{res},\alpha\neq 0} + 2\sqrt{\rho_{\mathrm{c}}\rho_{\mathrm{sb}}}t_{\mathrm{res},\alpha=0}(t_{\mathrm{res},\alpha=0} - t_{\mathrm{res},\alpha\neq 0})\cos(\Omega t)) \ . \tag{4.25}$$

We can write $t_{\mathrm{res},\alpha\neq 0}$ by substituting Eq. 2.16 into Eq. 2.23 and expanding for small αL[9]:

$$t_{\mathrm{res},\alpha\neq 0} \approx \frac{\mathcal{F}\tilde{t}_1\tilde{t}_2}{\pi} - \frac{\mathcal{F}^2\tilde{t}_1\tilde{t}_2\alpha L}{\pi^2} \ , \tag{4.26}$$

so the detected signal proportional to the beat RMS will be (see Page 21):

$$i_{\mathrm{signal,NICEsb}} = \sqrt{2}\eta\epsilon P_{\mathrm{in}}\sqrt{\rho_{\mathrm{c}}\rho_{\mathrm{sb}}}\,\frac{\mathcal{F}^3\tilde{t}_1^2\tilde{t}_2^2\alpha L}{\pi^3} \ . \tag{4.27}$$

As with the other detection schemes, the photocurrent shot-noise depends on the total average power at the detector, and here is given by

$$\langle S_i\rangle_{\mathrm{NICEsb}} = \sqrt{2e\eta P_{\mathrm{d}}} = \sqrt{2e\eta\epsilon P_{\mathrm{in}}t^2_{\mathrm{res}}} \tag{4.28}$$

$$\approx \frac{\mathcal{F}\tilde{t}_1\tilde{t}_2}{\pi}\sqrt{2e\eta\epsilon P_{\mathrm{in}}} \ , \tag{4.29}$$

remembering that all three modes (carrier and two sidebands) are resonant to the cavity, and t_{res} is given by Eq. 2.23. Equations 4.1, 4.27 and 4.28 give:

$$\langle S_\alpha\rangle_{\mathrm{NICEsb}} = \frac{\pi^2}{\mathcal{F}^2 L\tilde{t}_1\tilde{t}_2}\frac{1}{\sqrt{\epsilon P_{\mathrm{in}}\rho_{\mathrm{c}}\rho_{\mathrm{sb}}}}\sqrt{\frac{e}{\eta}} \tag{4.30}$$

$$\approx \frac{\pi}{\mathcal{F}L}\frac{1}{\sqrt{\epsilon P_{\mathrm{in}}\rho_{\mathrm{c}}\rho_{\mathrm{sb}}}}\sqrt{\frac{e}{\eta}} \qquad \text{(for } \delta \to 0,\ \tilde{t}_1\tilde{t}_2 \to \pi/\mathcal{F}) \ . \tag{4.31}$$

[9]As a reminder, $\tilde{t}_i$ represents the mirror amplitude transmissivity of a symmetric cavity (most commonly used in transmission-based detection setups) with same finesse as an asymmetric cavity with mirror transmissivity t_i.

In terms of $P_{\text{circ}} = \rho_{\text{circ}}\epsilon P_{\text{in}}$,

$$\langle S_\alpha \rangle_{\text{NICEsb}} = \frac{\pi}{\mathcal{F}L\tilde{t}_2} \frac{1}{\sqrt{P_{\text{circ}}\rho_{\text{c}}\rho_{\text{sb}}}} \sqrt{\frac{e}{\eta}} \ . \tag{4.32}$$

4.4.1 Comparing SideCAR to NICE-OHMS

Comparing Eqs. 4.13 and 4.30 for measurements with same cavity finesse and same *incoming power*, we get[10]

$$\left(\frac{\langle S_\alpha \rangle_{\text{SideCAR}}}{\langle S_\alpha \rangle_{\text{NICEsb}}} \right)_{P_{\text{in}}} = \frac{\tilde{t}_1 \tilde{t}_2}{t_1^2} \frac{1}{\sqrt{\epsilon}} \tag{4.33}$$

$$= \frac{1}{2\sqrt{\epsilon}} \tag{4.34}$$

where again we use $\tilde{t}_1 = \tilde{t}_2 = t_1/\sqrt{2}$ for the case of cavities with same finesse. When comparing them for the same *circulating power*, we get:

$$\left(\frac{\langle S_\alpha \rangle_{\text{SideCAR}}}{\langle S_\alpha \rangle_{\text{NICEsb}}} \right)_{P_{\text{circ}}} = \sqrt{\frac{\rho_{\text{sb}}}{2\epsilon}} \ . \tag{4.35}$$

If we were to consider NICE-OHMS with the carrier probing a sample resonance (see Footnote 10),

$$\left(\frac{\langle S_\alpha \rangle_{\text{SideCAR}}}{\langle S_\alpha \rangle_{\text{NICEc}}} \right)_{P_{\text{in}}} = \frac{1}{\sqrt{\epsilon}} \qquad \text{and} \qquad \left(\frac{\langle S_\alpha \rangle_{\text{SideCAR}}}{\langle S_\alpha \rangle_{\text{NICEc}}} \right)_{P_{\text{circ}}} = \sqrt{\frac{2\rho_{\text{sb}}}{\epsilon}} \ . \tag{4.36}$$

In the weak modulation regime (small ρ_{sb}) and with reasonable coupling ϵ to the cavity, there is a clear advantage in the sideband reflection shot-noise-limited sensitivity when a small circulating power is desired, even when using the carrier as a probe for NICE-OHMS (Fig. 4.2).

[10] Note again that I am using the NICE-OHMS case with sideband interaction, not carrier. Although carrier interaction is optimized (gives sensitivity 2 times better than sideband interaction), it can only give a dispersion signal, and the equation given in literature for the dispersion case contains undesired approximations of $\delta \to 0$. So when comparing the optimized SideCAR with optimized NICE-OHMS (carrier), at the limit of $r_1 \to 1$ and $\epsilon \to 1$, the sensitivity floor of the two techniques is the same (Eq. 4.36). Note also that for a carrier interaction and in the limit of $\delta \to 0$, the results derived here give

$$\langle S_\alpha \rangle_{\text{NICEc}} = \frac{\pi}{2\mathcal{F}L} \frac{1}{\sqrt{\epsilon P_{\text{in}}\rho_{\text{c}}\rho_{\text{sb}}}} \sqrt{\frac{e}{\eta}} \ .$$

This result differs from Ye et al. [10], Ma et al. [11] by a factor of 1/2.

We note however that NICE-OHMS is intrinsically noise-immune and therefore can indeed achieve the shot-noise limit, while our reflection technique suffers from classical noise (see Section 5.4). Nonetheless, we can still achieve comparable experimental noise floors over a frequency range relevant to detection of $\sim$ µs transients, but with a much lower intracavity power, which might be important to avoid nonlinearities in the intracavity medium. Also, the possibility of single-port measurements can be useful for practical sensors.

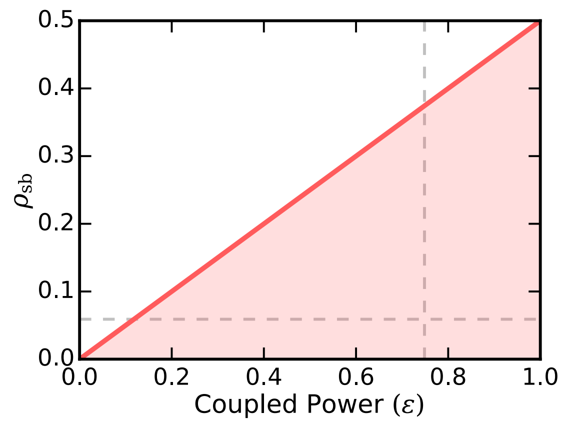

Figure 4.2: Comparing the shot-noise-limited sensitivity of SideCAR $\langle S_\alpha \rangle_{\rm SideCAR}$ to that acquired with the optimized NICE-OHMS measurement $\langle S_\alpha \rangle_{\rm NICEc}$, for cavities of same finesse and same circulating power (Eq. 4.36). Coral curve shows the points of equal sensitivity $\langle S_\alpha \rangle_{\rm SideCAR} = \langle S_\alpha \rangle_{\rm NICEc}$. Shaded area illustrates the region where there is an advantage in using SideCAR (if shot-noise-limited). Dashed grey lines mark our experimental parameters ($\epsilon = 0.749$, $\rho_{\rm sb} = 0.0590$).

Chapter 5

Experimental setup and results

In an experimental setup, there are many sources of technical noise that usually do not allow us to reach the quantum-limited absorption sensitivity derived in Chapter 4. We performed a set of experiments using a 5-cm long optical cavity to test the validity of the proposed sensing technique, and to measure real-world noise floors. The signal that we measure in the laboratory is a voltage V_X, related to the heterodyne reflection beat amplitude by $V_X \equiv G_X P_X$ (Section 3.2). Following the same idea from Chapter 4, the experimental noise-equivalent absorption sensitivity can be found by the noise present in the measurement of V_X scaled by $|dV_X/d\alpha|$, which can be determined from Eqs. 2.16 and 3.6:

$$\left|\frac{dV_X}{d\alpha}\right| = \frac{2\mathcal{F}^2 L t_1^2}{\pi^2}|G_X| P_{\mathrm{in}}\epsilon\sqrt{\rho_{\mathrm{c}}\rho_{\mathrm{sb}}}\ . \tag{5.1}$$

Thus, in order to determine the experimental sensitivity, we need to know all the following parameters: front and back mirror amplitude reflectivities r_1 and r_2 (or equivalently power transmissivities $t_i^2 = 1 - r_i^2$); cavity length L; cavity intrinsic losses δ (or equivalently the cavity lifetime τ – Eq. 2.17); the factor G_X that involves all gains in the path from the cavity until the measurement of V_X (i.e., optical power gains G_{opt} from cavity to detector, detector gain G_{d} in V/W and mixing circuitry voltage gains G_{mix}); cavity input power P_{in}; power coupling parameter ϵ; and fractional carrier and sideband powers ρ_{c} and ρ_{sb}. Sections 5.1 to 5.3 detail our experimental apparatus and the measurements performed in order to characterize all these setup gains and parameters. It all comes together in Section 5.4, where we present the noise-equivalent absorption sensitivity of this experiment.

5.1 Apparatus

The apparatus used for our sideband locking and sensing technique is represented in Fig. 5.1. A 1550-nm continuous-wave laser is phase-modulated at frequency $\Omega/(2\pi) \sim 1$ GHz with an electro-optical modulator (EOM) controlled by a voltage-controlled oscillator (VCO). The phase-modulated signal is outcoupled via a fiber collimator, propagates in free space through a non-polarizing 50-50 beamsplitter (BS) and reaches a 5-cm long optical cavity

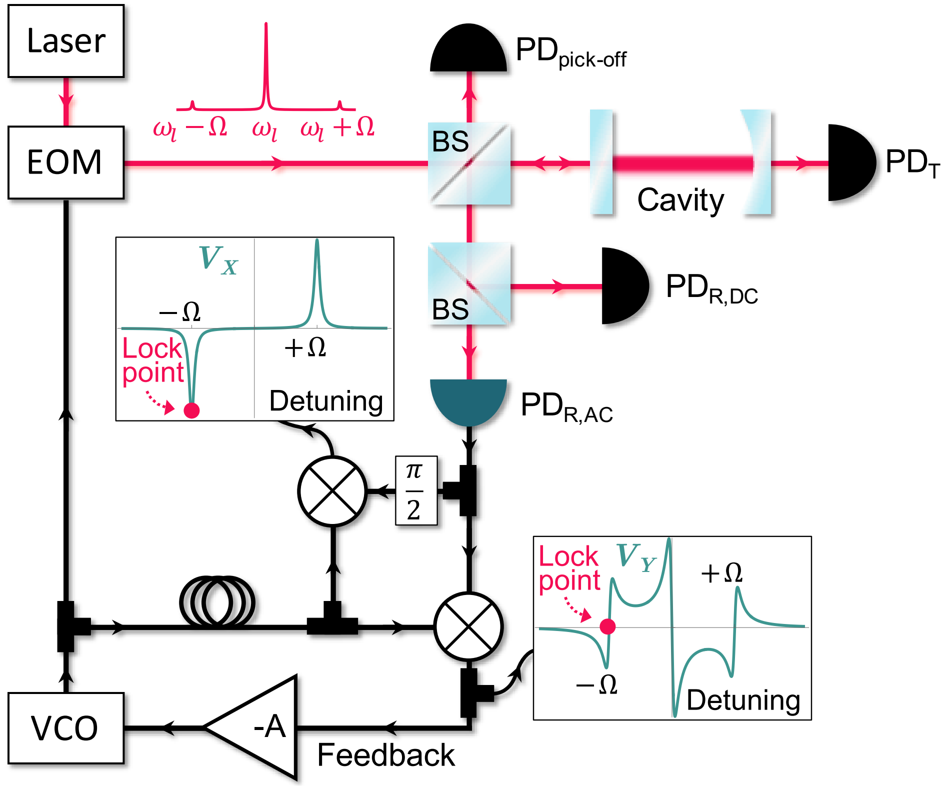

Figure 5.1: Experimental setup for sideband PDH locking and cavity-enhanced absorption readout. Laser light at frequency ω_l is phase-modulated at Ω by an EOM, generating two sidebands at $\omega_l \pm \Omega$. When one of the tones is resonant with an optical cavity, the triplet is disturbed and generates a heterodyne beat that is collected by an AC-coupled photodetector ($\text{PD}_{R,\text{AC}}$) and demodulated with a reference at Ω. Insets show PDH out-of-phase (*amplitude*) quadrature (V_X) and in-phase (*phase*) quadrature (V_Y). Red dots indicate the lock point on the lower sideband. Three DC-coupled photodetectors are used for setup diagnosis and measurement of system parameters. EOM: electro-optical modulator. BS: non-polarizing beamsplitter. PD: photo-detector (T: transmission, R: reflection). VCO: voltage-controlled oscillator. -A: feedback controller. $\pi/2$ indicates a phase shift.

formed by a flat input mirror and a concave back mirror. We collect the other half of the signal from the BS with a pick-off DC-coupled photodetector ($\text{PD}_{\text{pick-off}}$). This signal is used to normalize all other collected signals in terms of cavity input power P_{in}. The transmitted light is also collected with a second photodetector (PD_T). The reflected light goes back through the BS and is directed to a second non-polarizing 50-50 BS. Half of the signal is collected by a third DC-coupled photodetector ($\text{PD}_{R,\text{DC}}$). The three detectors $\text{PD}_{\text{pick-off}}$, PD_T and $\text{PD}_{R,\text{DC}}$ are the ThorLabs PDA10CF (bandwidth DC – 150 MHz). The other half of the reflected signal is collected by an AC-coupled fast detector $\mathrm{PD}_{R,\mathrm{AC}}$ (FEMTO HSA-X-S-2G-IN, bandwidth 10 kHz – 2 GHz), which is fast enough to measure the heterodyne beat (at frequency Ω) generated by the PDH reflection. The AC voltage signal is then split again: half of it is demodulated with an in-phase reference signal at Ω coming from the VCO, while the other half is phase-shifted before being mixed with the same reference. The in-phase mixed signal $V_Y \propto P_Y$ (Eq. 3.4) is sent to a feedback controller and fed back to the VCO, so it controls the sideband frequency, keeping the lower sideband locked on resonance with the cavity (Section 3.1). A delay line is added between the VCO and mixer LO port to ensure the LO and RF signals have the same delay, ensuring stable relative phase even when the VCO frequency changes. The out-of-phase mixed signal V_X is acquired and used to monitor changes in intracavity absorption α (Section 3.2).

5.2 System parameters

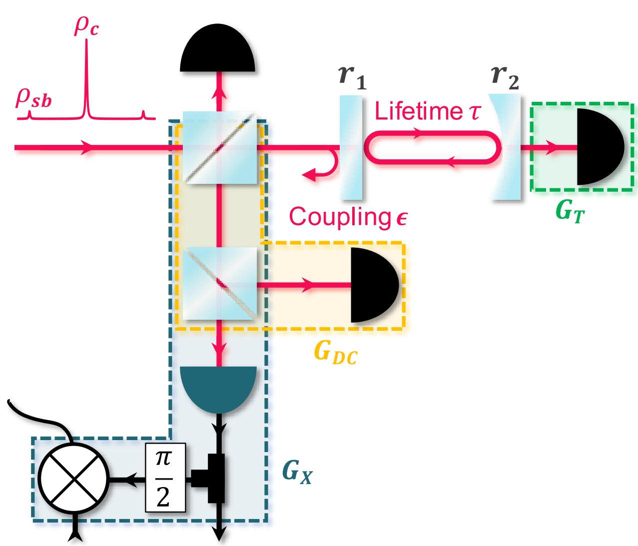

Figure 5.2: Schematic of the parameters extracted from measurements and simultaneous fit. Transmission and reflection detectors are used to perform independent measurements to extract system parameters, namely: carrier and sideband relative power ρ_{c} and ρ_{sb}, front and back mirror amplitude reflectivity r_1 and r_2, power coupling parameter ϵ, empty cavity lifetime τ, and the gain factors in the three signal paths: transmission (G_T), DC reflection (G_{DC}) and beatnote reflection (G_X). All measurements are normalized for the cavity input power P_{in} using a pick-off detector.

We perform a set of measurements using the voltage readings of four photodetectors depicted in Fig. 5.2 to extract all our unknown system parameters. The cavity length L, the input mirror fractional transmitted power t_1^2 (which gives $r_1 = \sqrt{1-t_1^2}$) and the transmission path gain factor $G_T = V_T/P_T$ (where V_T is the transmission-diode voltage reading and P_T is the average power transmitted by the cavity) are directly measured. By quickly sweeping the cavity length by means of a piezo-mounted back mirror, we take swept ringdown measurements to extract the empty cavity lifetime τ (Fig. 5.3a). In addition, by sweeping the cavity length more slowly, we acquire a set of five measurements: cavity reflection V_R and transmission V_T without phase modulation, cavity reflection with phase modulation around the carrier $V_{R\mathrm{c}}$ and the lower sideband resonance $V_{R\mathrm{sb}}$, and the demodulated PDH amplitude quadrature V_X around the lower sideband resonance (Fig. 5.3b-f). These five measurements are then simultaneously fitted to extract the remaining parameters (carrier and sideband relative power ρ_c and ρ_sb, back mirror amplitude reflectivity r_2, power coupling parameter ϵ, and the gain factors in the DC (G_DC) and beat (G_X) reflection paths). To account for incoming power fluctuations, we normalize the voltage sweeps using the readings from the pick-off diode. The swept ringdown measurements are fitted with the function [9, 26]:

$$V_\mathrm{RD} = ae^{-t/2\tau}\cos\left((\omega + bt)t + c\right) + d + gt + ht^2 \ . \tag{5.2}$$

The equations for the simultaneous fits are:

$$\frac{V_R}{P_\mathrm{in}} = G_\mathrm{DC}\Big((1-\epsilon)r_1^2 + \epsilon R(\Delta L)\Big) \tag{5.3}$$

$$\frac{V_T}{P_\mathrm{in}} = G_T\epsilon T(\Delta L) \tag{5.4}$$

$$\frac{V_{R\mathrm{c}}}{P_\mathrm{in}} = G_\mathrm{DC}\Big((1-\epsilon)r_1^2 + \epsilon(\rho_\mathrm{c}R(\Delta L) + 2\rho_\mathrm{sb}r_1^2)\Big) \tag{5.5}$$

$$\frac{V_{R\mathrm{sb}}}{P_\mathrm{in}} = G_\mathrm{DC}\Big((1-\epsilon)r_1^2 + \epsilon(\rho_\mathrm{c}r_1^2 + \rho_\mathrm{sb}r_1^2 + \rho_\mathrm{sb}R(\Delta L))\Big) \tag{5.6}$$

$$\frac{V_X}{P_\mathrm{in}} = 2G_X\epsilon\sqrt{\rho_\mathrm{c}\rho_\mathrm{sb}}\,\Big(r_1^2 + r_1\,\mathrm{Re}\{r(\Delta L)\}\Big) \tag{5.7}$$

with $r(\Delta L)$, $R(\Delta L)$ and $T(\Delta L)$ given by expanding Eqs. 2.10, 2.12 and 2.13 around a small cavity length detuning from resonance ΔL and using the high finesse limit approximation:

$$r(\Delta L) \approx \frac{t_1^2}{\frac{\pi}{\mathcal{F}} - 2i\Delta L n\omega/c} - r_1 \tag{5.8}$$

$$R(\Delta L) \approx \frac{t_1^4 - 2\pi r_1 t_1^2/\mathcal{F}}{\frac{\pi^2}{\mathcal{F}^2} + (2\Delta L n\omega/c)^2} + r_1^2 \tag{5.9}$$

$$T(\Delta L) \approx \frac{t_1^2 t_2^2}{\frac{\pi^2}{\mathcal{F}^2} + (2\Delta L n\omega/c)^2}, \tag{5.10}$$

setting $\omega \approx \omega_l$ and the time-dependent displacement from resonance $\Delta L = v_a(v_b t^2 + t - t_0)$. v_a and v_b are fit parameters that account for the nonlinear displacement of the piezo with time, and t_0 is a fit time offset. The resulting values for all the setup parameters are given in Table 5.1. The intracavity medium (air) index of refraction n is set to 1.

Parameter	Experimental Value
L	5.19 ± 0.10 cm
τ	495.9 ± 0.2 ns
ϵ	0.749 ± 0.005
r_1	0.999796 ± 0.000006
r_2	0.9999974 ± 0.0000001
$\mathcal{F}$	9006 ± 174
δ	$(143 \pm 9) \times 10^{-6}$
ρ_{c}	0.8831 ± 0.0007
ρ_{sb}	0.0590 ± 0.0003
G_T	3014 ± 159 V/W
G_{DC}	364 ± 9 V/W
G_X	-80 ± 3 V/W

Table 5.1: Experimental parameters. L, $r_1 = \sqrt{1 - t_1^2}$ and G_T are directly measured. τ, ϵ, r_2, ρ_{c}, ρ_{sb}, G_{DC} and G_X are extracted from the fit of a set of measurements (see text). $\mathcal{F} = \pi c\tau/(Ln)$ (Eq. 2.14) and Eq. 2.17 give the cavity finesse $\mathcal{F}$ and intrinsic losses δ, respectively.

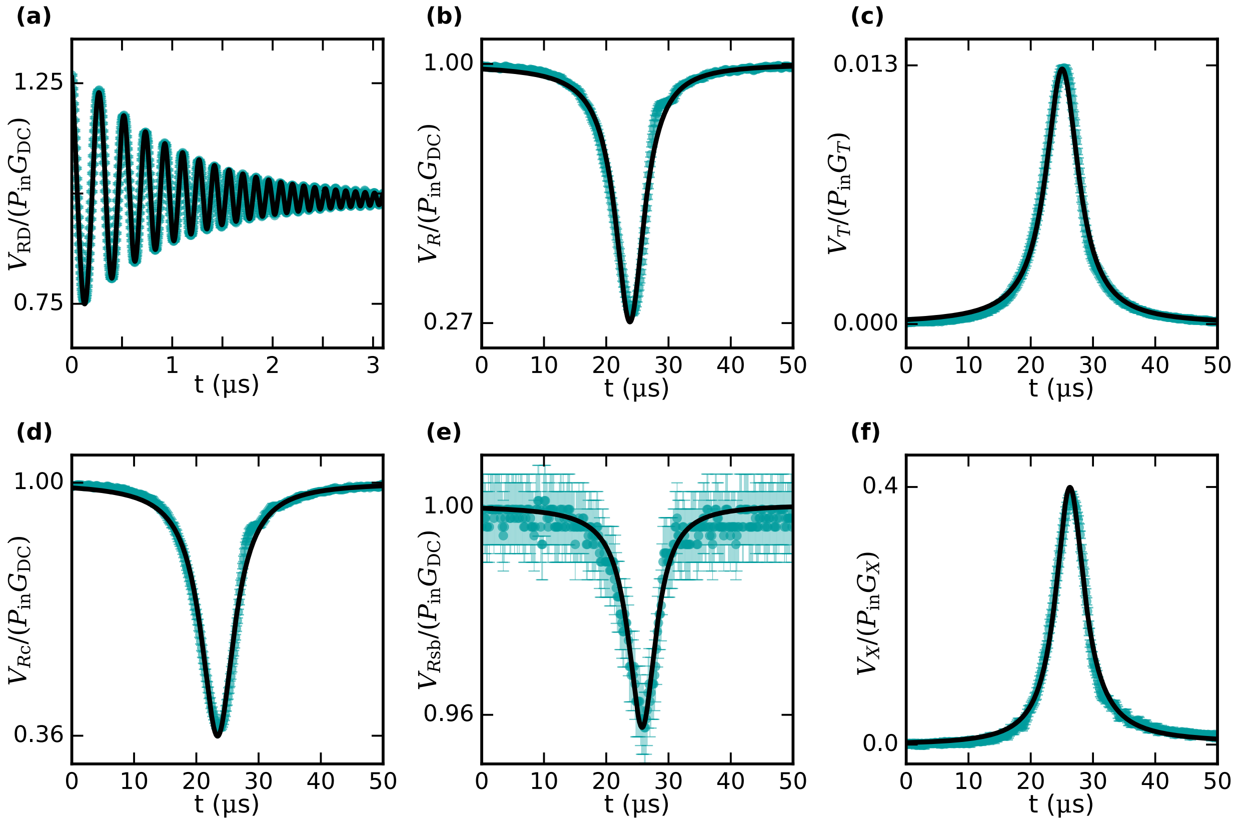

Figure 5.3: Empty cavity characterization with simultaneous fits. We extract system parameters (cavity lifetime τ, gain factors G_{DC} and G_X, power coupling parameter ϵ, back mirror amplitude reflectivity r_2, and carrier and sideband relative power ρ_{c} and ρ_{sb}) by simultaneously fitting a set of six cavity length sweep measurements: (a) swept ring-down spectroscopy V_{RD}; (b) cavity reflection V_R (without sidebands); (c) cavity transmission V_T (without sidebands); (d) modulated reflection around the carrier resonance $V_{R\mathrm{c}}$; (e) modulated reflection around the lower sideband resonance $V_{R\mathrm{sb}}$; and (f) demodulated PDH beat signal V_X. We observe a small divergence between fit and data in the right-hand side of the peaks of the slow sweep measurements (b-f), due to residual ring-down from intracavity light even at small ($\sim$ 10 Hz) sweeping frequencies, not accounted for in the fit equations.

5.3 Mixing circuit gain

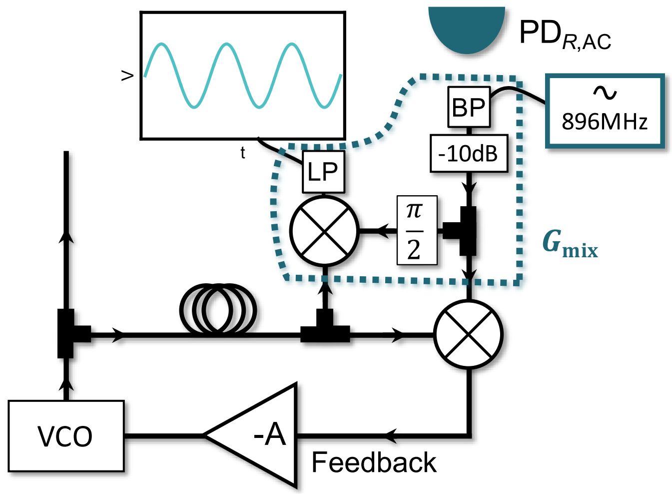

Figure 5.4: Characterization of mixing circuitry gain. A signal coming from a signal generator replacing the fast photodetector is collected after mixing. BP: band-pass filter. LP: low-pass filter.

In the detection setup, the signal collected by the fast detector goes through a band pass filter (20-1000 MHz), a -10 dB attenuator, a $\pi/2$ splitter, a mixer and an 11 MHz low-pass filter (components inside teal dashed box in Fig. 5.4). Although we could extract this mixer circuitry gain G_{mix} from $G_X = G_{\mathrm{opt}} G_{\mathrm{d}} G_{\mathrm{mix}}$ using the detector nominal gain G_{d} in V/W and G_{opt} (that is easily measured from the ratio of the readings of a power meter in front of PD$_{R,\mathrm{AC}}$ and in front of the cavity), we measured it experimentally as a check (which also serves as a check that the detector true gain agrees with specs, giving $G_{\mathrm{d}} = 4.8 \pm 0.2$ V/mW versus a nominal gain of 4.75 V/mW). The total gain of these circuit components was measured by replacing the fast detector output by an RF signal of known amplitude at the modulation frequency ($\Omega/(2\pi) \approx 896$ MHz), and monitoring the amplitude of the mixer + low-pass output. In our case, the voltage gain was found to be $G_{\mathrm{mix}} = 0.094 \pm 0.002$. The signal (in V) detected by the fast detector is scaled by G_{mix}, while the noise (in V/$\sqrt{\mathrm{Hz}}$) is scaled by $\sqrt{2} G_{\mathrm{mix}}$, since the mixing doubles the power noise (see Page 21).

5.4 Experimental results

As detailed in Chapter 4, the absorption sensitivity of our measurement can be found by the noise present in the measurement of V_X scaled by $dV_X/d\alpha$[11]. While in principle we have a theoretical prediction for $dV_X/d\alpha$ given by Eq. 5.1 that we can evaluate with the cavity parameters extracted with the measurements described in Section 5.2, we perform an independent calibration as a check (Fig. 5.5b). Note that, using Eq. 2.17:

$$\frac{dV_X}{d\alpha} = \frac{dV_X}{d\tau}\frac{d\tau}{d\alpha} \qquad \text{and} \qquad \left|\frac{d\tau}{d\alpha}\right| = \frac{c\tau^2}{n}, \tag{5.11}$$

where c is the speed of light and n is the index of refraction of the intra-cavity medium. Thus, by measuring $dV_X/d\tau$, i.e. how the measured voltage and measured cavity lifetime vary as we change the absorption, we can experimentally calibrate our sensitivity.

In Fig. 5.5a, we plot the measured noise power spectrum of V_X (in units of V^2/Hz) from 160 μW coupled to the cavity (corresponding to the power $\epsilon\rho_{\mathrm{sb}}P_{\mathrm{in}}$ in the resonant lower sideband, from a total $P_{\mathrm{in}} = 3.55$ mW landing on the cavity), and 520 mW circulating power. From this circulating power, only 38 μW land on the $\mathrm{PD}_{R,\mathrm{AC}}$ (due to losses to the two BS). The "locked" data (coral) shows the V_X signal that carries information on the intracavity absorption. For comparison, we plot the noise in V_X when the cavity is unlocked (laser and electronics noise – teal curve), the noise from electronics added to a shot-noise-limited laser (dotted yellow – calculated) and the theoretical shot noise limit (SNL) itself (dotted black – calculated as per Footnote 11).

Figure 5.5b shows the measured values of V_X (normalized using the voltage readings of a pick-off diode to account for power fluctuations) and cavity lifetime τ as we marginally occlude the cavity mode with a block of anodized aluminum, thereby changing the absorption in the cavity. As expected from the high-finesse relationship given by Eq. 3.6

[11] Note that in this chapter we consider voltage amplitude measurements ($\propto P_X$) and voltage shot noise limit $\langle S_V\rangle$, where in Chapter 4 we considered current RMS signals i_{signal} ($\propto \sqrt{\langle P_X\cos(\Omega t)\rangle^2}$) and current shot noise limit $\langle S_i\rangle$ (Eq. 4.2), for simplicity. The two quantities are simply related by

$$\langle S_V\rangle = \sqrt{2}G_{\mathrm{mix}}Z\langle S_i\rangle = 2G_{\mathrm{mix}}Z\sqrt{e\eta\bar{P}_{\mathrm{d}}}\ ,$$

where G_{mix} is the voltage gain of the mixing circuitry (Section 5.3), Z is the detector transimpedance in V/A and the extra $\sqrt{2}$ factor comes from the unavoidable doubling in power noise due to mixing. The two treatments are equivalent, since when dealing with currents the same factor of $\sqrt{2}$ arrises from "collecting" the current RMS.

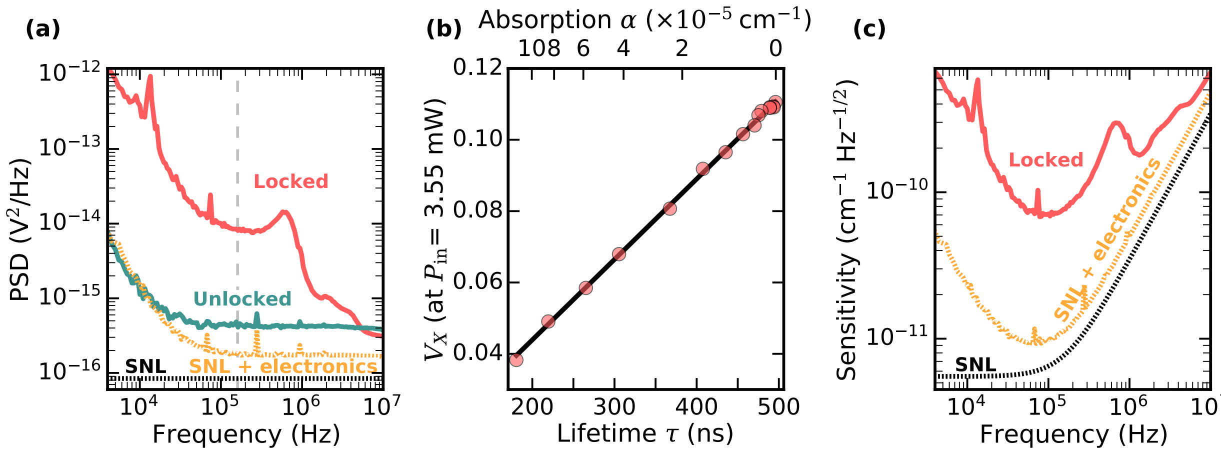

Figure 5.5: Experimental results. (a) Measurement noise spectrum (power spectral densities – PSDs). Coral: noise floor of the system (V_X) while laser is locked to the cavity. Teal: unlocked laser noise. Dotted yellow: shot-noise limit (SNL) and electronics noise. Dotted black: SNL (experimental quantum limit). The vertical dashed line marks our V_X measurement bandwith $1/(4\pi\tau) = 160$ kHz. (b) Calibration of voltage measurement V_X (normalized) vs. cavity lifetime τ. Black line is a fit to data (coral). As expected, we observe a linear relation between V_X and τ (Eq. 5.12), supported by the linear fit R^2 of 0.99894. Top axis shows predicted α-dependence of V_X $\left(\alpha = -\frac{t_1^2+t_2^2+2\delta}{2L} + \frac{n}{c\tau}\right)$. (c) Conversion of the voltage measurement from (a) to sensitivity using the calibration from (b). We correct our locked measurement of V_X for the cavity transfer function (low pass behaviour). We currently achieve noise-equivalent absorption sensitivities below 10^{-10} cm$^{-1}/\sqrt{\text{Hz}}$ from 30 to 200 kHz and a minimum of 7×10^{-11} cm$^{-1}/\sqrt{\text{Hz}}$ at ~ 100 kHz, a factor of 11 from the SNL, due to classical amplitude noise in the laser and frequency noise from the locking technique.

and $V_X = G_X P_X$ [12], and substituting $\mathcal{F} = \omega_{\text{FSR}} \cdot \tau = \pi c\tau/(Ln)$ (Eq. 2.14),

$$V_X = 2G_X \epsilon P_{\text{in}} \sqrt{\rho_c \rho_{\text{sb}}}\, \frac{t_1^2 c\tau}{Ln} \tag{5.12}$$

depends linearly on τ. The slope of the fitted data[13] $dV_X/d\tau = 225.5 \pm 0.3$ mV/µs agrees with the theoretical value of 227 ± 14 mV/µs evaluated from Eq. 5.12 for our system parameters (Table 5.1). The linear relation between V_X and τ is also confirmed by the fit R^2 equal to 0.99894.

[12] As a reminder, G_X contains all the gains in the AC detector path from the cavity until acquisition, including the optical power losses between cavity and detector, detector gain $G_d = Z\eta$ in V/W and circuitry voltage gains G_{mix}.

[13] V_X calibration measurements are scaled to what they would be for an incoming power $P_{\text{in}} = 3.55$ mW (the average P_{in} during locked PSDs acquisition) by multiplying by 3.55 mW over the measured input power.

The results of Fig. 5.5a and Fig. 5.5b are combined with the measurement bandwidth to determine the absorption sensitivity of our apparatus. In principle, the voltage power spectrum can be converted to sensitivity (in $\mathrm{cm}^{-1}/\sqrt{\mathrm{Hz}}$) by scaling the square root of the PSDs ($\mathrm{V}/\sqrt{\mathrm{Hz}}$) by $dV_X/d\alpha$ ($\mathrm{V}/\mathrm{cm}^{-1}$), using the calibration from Fig. 5.5b and Eq. 5.11. However, as detailed in Section 3.3, the cavity imposes a low-pass filter with cutoff frequency $1/4\pi\tau = 160$ kHz on the absorption signal, increasing the impact of noise at higher frequencies. The resulting noise-equivalent absorption sensitivity (corrected for the cavity response) is shown by the coral curve in Fig. 5.5c, along with the SNL (dotted black) and electronic noise + SNL (dotted yellow) for comparison. Over the $30 - 200$ kHz frequency range, we observe a noise-equivalent absorption sensitivity below 10^{-10} $\mathrm{cm}^{-1}/\sqrt{\mathrm{Hz}}$, with a minimum of 7×10^{-11} $\mathrm{cm}^{-1}/\sqrt{\mathrm{Hz}}$ at ~ 100 kHz, a factor of 11 from the SNL.

By comparing the locked (coral) and unlocked (teal) curves in Fig. 5.5a, we observe that the excess noise occurs primarily in the transition from unlocked to sideband-locked operation. Due to the mixing with a reference at the modulation frequency $\Omega \sim 2\pi \cdot 1$ GHz (see Fig. 5.1), when unlocked, V_X measures laser noise at frequencies $\Omega < \omega < \Omega + 2\pi \cdot 11\mathrm{MHz}$, with the 11 MHz bandwidth dictated by a low-pass filter after the mixer. In contrast, when locked, the collected signal beats at Ω, so mixing V_X detects the true laser noise at the plotted frequency ($0 < \omega/2\pi < 11$ MHz). This measurement is sensitive to low-frequency laser noise (at the plotted frequency), and other sources including laser frequency noise (detuning from cavity resonance), VCO frequency noise and cavity length noise. Fluctuations in cavity length or laser frequency change the resonance condition, detuning the cavity and also changing the modulation frequency Ω via the feedback loop. If the VCO output power varies with Ω, it results in amplitude noise in V_X from changes in the modulation amplitude (fluctuations in $\sqrt{\rho_{\mathrm{sb}}}$). We investigate these noise sources by simultaneously acquiring voltages from the pick-off diode, feedback controller error monitor and VCO output (using a crystal detector to collect the VCO output power). The noise spectra of the four measurements are plotted in Fig. 5.6. We can identify many of the features in V_X coming from the other sources. Current work is being done towards subtraction of these three noise sources from V_X.

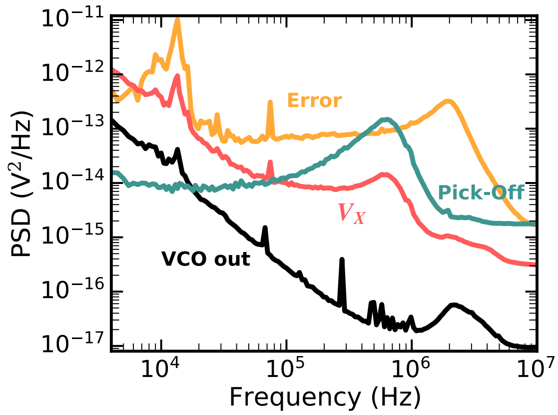

Figure 5.6: Investigating features in V_X noise spectrum. Noise spectrum in four simultaneously acquired locked measurements: V_X (coral), feedback controller error monitor (yellow), pick-off diode (teal) and VCO output power (black). We can identify the features appearing in V_X from the other measurements, e.g.: the known laser amplitude noise peak around 500 kHz in the pick-off measurement; the peak around the feedback loop bandwidth (~ 2 MHz) in the feedback controller (Error); and the low-frequency noise likely arising from cavity length drifts in the VCO output power.

Chapter 6

Conclusion and Outlook

This thesis details the work done towards the development of a new absorption sensor that works in reflection and is capable of detecting both narrow and broad absorption features, with high sensitivity within a large bandwidth. We showed that the robust PDH sideband locking scheme enables a simultaneous absorption measurement with the readout of the amplitude quadrature of a heterodyne reflection beat, which varies linearly with cavity lifetime. By monitoring this signal, we can detect transients with a bandwidth set by the cavity amplitude decay rate. We developed a model of the measurement that allows us to quantitatively predict its shot-noise-limited performance, showing that its sensitivity floor is comparable to standard transmission measurements. Finally, we demonstrated the method with a test air-filled 5-cm-long cavity, finding a noise-equivalent absorption sensitivity $\sim 10^{-10}$ cm$^{-1}/\sqrt{\text{Hz}}$ in the $30-200$ kHz range, and a minimum of 7×10^{-11} cm$^{-1}/\sqrt{\text{Hz}}$ at 100 kHz without system optimization, while maintaining the cavity locked to a modulation sideband with a coupled power of 160 μW. This sensitivity is a factor of 11 from the shot-noise limited sensitivity. The use of a shot-noise-limited laser, lower noise VCO and electronic components and the current work being done towards subtraction of classical noise will allow us to further approach this quantum limit.

The project was motivated by the proposal of developing a solvated electron dosimeter for radiotherapy applications [27]. Solvated electrons are entities formed upon hydrolysis (following water irradiation) that exhibit broad optical absorption in the visible and near infrared [4, 5]. This signal persists only for a few microseconds and is hidden by a strong background absorption of the water medium in the same spectral range. Up until today, dosimetry in radiotherapy is mostly done using radiographic films placed at a distance (external to the body) of the aimed irradiated tissue, which results in poor sensitivity and lack of spacial resolution. Radiographic films also forbid a real-time dose assessment, since the films are only verified after the irradiation session. Our locked measurement will allow the detection of transients in real time. The possibility of measuring reflection from a micrometer-scale fiber cavity [28] lets us envision the design of a sensor placed at the tip of an endoscope, giving spatially-resolved measurements from a low-power probe with enough sensitivity (boosted by heterodyne detection) to detect the relatively small solvated electron absorption signal in the noisy absorptive background. For applications that require a high-bandwidth lock, low-power probe, or reflection-based detection, this approach could replace a range of transmission-based cavity-enhanced absorption sensing schemes, and could facilitate sensitive detection of transient absorption features with close to shot-noise-limited sensitivity.

Bibliography

[1] D. Romanini, I. Ventrillard, G. Méjean, J. Morville, and E. Kerstel, "Introduction to cavity enhanced absorption spectroscopy," in *Cavity-Enhanced Spectroscopy and Sensing.* Springer, 2014, pp. 1–60.

[2] E. D. Black, "An introduction to Pound–Drever–Hall laser frequency stabilization," *American Journal of Physics*, vol. 69, no. 1, pp. 79–87, 2001.

[3] C. Reinhardt, T. Müller, and J. C. Sankey, "Simple delay-limited sideband locking with heterodyne readout," *Optics Express*, vol. 25, no. 2, pp. 1582–1597, 2017.

[4] E. J. Hart and J. Boag, "Absorption spectrum of the hydrated electron in water and in aqueous solutions," *Journal of the American Chemical Society*, vol. 84, no. 21, pp. 4090–4095, 1962.

[5] J. M. Herbert and M. P. Coons, "The hydrated electron," *Annual Review of Physical Chemistry*, vol. 68, pp. 447–472, 2017.

[6] M. Mazurenka, A. J. Orr-Ewing, R. Peverall, and G. A. Ritchie, "4. Cavity ring-down and cavity enhanced spectroscopy using diode lasers," *Annual Reports Section C (Physical Chemistry)*, vol. 101, pp. 100–142, 2005.

[7] J. M. Herbelin and J. A. McKay, "Development of laser mirrors of very high reflectivity using the cavity-attenuated phase-shift method," *Applied Optics*, vol. 20, no. 19, pp. 3341–3344, 1981.

[8] A. O'Keefe and D. A. Deacon, "Cavity ring-down optical spectrometer for absorption measurements using pulsed laser sources," *Review of Scientific Instruments*, vol. 59, no. 12, pp. 2544–2551, 1988.

[9] Y. He and B. Orr, "Rapidly swept, continuous-wave cavity ringdown spectroscopy with optical heterodyne detection: single- and multi-wavelength sensing of gases," *Applied Physics B*, vol. 75, no. 2-3, pp. 267–280, 2002.

[10] J. Ye, L.-S. Ma, and J. L. Hall, "Ultrasensitive detections in atomic and molecular physics: demonstration in molecular overtone spectroscopy," *Journal of the Optical Society of America B*, vol. 15, no. 1, pp. 6–15, 1998.

[11] L.-S. Ma, J. Ye, P. Dubé, and J. L. Hall, "Ultrasensitive frequency-modulation spectroscopy enhanced by a high-finesse optical cavity: theory and application to overtone transitions of C_2H_2 and C_2HD," *Journal of the Optical Society of America B*, vol. 16, no. 12, pp. 2255–2268, 1999.

[12] J. Hodgkinson and R. P. Tatam, "Optical gas sensing: a review," *Measurement Science and Technology*, vol. 24, no. 1, p. 012004, 2013.

[13] A. Maity, S. Maithani, and M. Pradhan, "Cavity ring-down spectroscopy: recent technological advancements, techniques, and applications," *Analytical Chemistry*, vol. 93, no. 1, pp. 388–416, 2021.

[14] J. Hu, F. Wan, P. Wang, H. Ge, and W. Chen, "Application of frequency-locking cavity-enhanced spectroscopy for highly sensitive gas sensing: a review," *Applied Spectroscopy Reviews*, pp. 1–33, 2021.

[15] T. Spence, C. Harb, B. Paldus, R. N. Zare, B. Willke, and R. Byer, "A laser-locked cavity ring-down spectrometer employing an analog detection scheme," *Review of Scientific Instruments*, vol. 71, no. 2, pp. 347–353, 2000.

[16] G. S. Engel, W. S. Drisdell, F. N. Keutsch, E. J. Moyer, and J. G. Anderson, "Ultrasensitive near-infrared integrated cavity output spectroscopy technique for detection of co at 1.57 μm: new sensitivity limits for absorption measurements in passive optical cavities," *Applied Optics*, vol. 45, no. 36, pp. 9221–9229, 2006.

[17] J. Dong, T. T.-Y. Lam, M. B. Gray, R. B. Warrington, E. H. Roberts, D. A. Shaddock, D. E. McClelland, and J. H. Chow, "Optical cavity enhanced real-time absorption spectroscopy of CO_2 using laser amplitude modulation," *Applied Physics Letters*, vol. 105, no. 5, p. 053505, 2014.

[18] J. Landsberg, D. Romanini, and E. Kerstel, "Very high finesse optical-feedback cavity-enhanced absorption spectrometer for low concentration water vapor isotope analyses," *Optics Letters*, vol. 39, no. 7, pp. 1795–1798, 2014.

[19] W. Zhang, X. Chen, X. Wu, Y. Li, and H. Wei, "Adaptive cavity-enhanced dual-comb spectroscopy," *Photonics Research*, vol. 7, no. 8, pp. 883–889, 2019.

[20] J. H. Chow, I. C. Littler, D. S. Rabeling, D. E. McClelland, and M. B. Gray, "Using active resonator impedance matching for shot-noise limited, cavity enhanced amplitude

modulated laser absorption spectroscopy," *Optics Express*, vol. 16, no. 11, pp. 7726–7738, 2008.

[21] G. R. Fowles, *Introduction to Modern Optics.* Dover, 1989.

[22] C. Stambaugh, H. Xu, U. Kemiktarak, J. Taylor, and J. Lawall, "From membrane-in-the-middle to mirror-in-the-middle with a high-reflectivity sub-wavelength grating," *Annalen der Physik*, vol. 527, no. 1-2, pp. 81–88, 2015.

[23] E. Hecht, *Optics, Fifth Edition.* Pearson Education, 2017.

[24] J. Ye and J. L. Hall, "3. Absorption detection at the quantum limit: probing high-finesse cavities with modulation techniques," in *Experimental Methods in the Physical Sciences.* Elsevier, 2003, vol. 40, pp. 83–127.

[25] W. Schottky, "Über spontane stromschwankungen in verschiedenen elektrizitätsleitern," *Annalen der physik*, vol. 362, no. 23, pp. 541–567, 1918.

[26] C. Reinhardt, T. Müller, A. Bourassa, and J. C. Sankey, "Ultralow-noise sin trampoline resonators for sensing and optomechanics," *Physical Review X*, vol. 6, no. 2, p. 021001, 2016.

[27] J. Mégrourèche, "Development of a hydrated electron dosimeter for radiotherapy applications: a proof of concept," Master's thesis, McGill University, 2020.

[28] D. Hunger, T. Steinmetz, Y. Colombe, C. Deutsch, T. W. Hänsch, and J. Reichel, "A fiber fabry–perot cavity with high finesse," *New Journal of Physics*, vol. 12, no. 6, p. 065038, 2010.